HABILITATION THESIS

Magnetization dynamics in solids studied by microscopic theory methods

RNDr. Karel Carva, Ph.D.

Condensed Matter Physics

Prague 2019

Contents

3

Preface

This habilitation thesis consists of a set of 26 author's published scientific works reprinted in the Appendix and a unifying commentary forming the thesis body. The selected works contribute in some degree to microscopic explanation of various phenomena related to evolution of magnetization, and I have authored or coauthored them in the course of last 12 years. In the text they are referenced as [A.#], where # is a number. From these publications I would like to stress out the extensive work on a chapter in the prestigious book series Handbook of Magnetic Materials. This contribution was requested by its Editor, and represents one of only two chapters in the year 2017 volume. Due to its extent of 172 pages only its contents and introduction is reprinted here.

Majority of the work was done in Prague at the Faculty of Mathematics and Physics of Charles University, Department of Condensed Matter, some earlier works originated during my 2 year postdoc stay at Uppsala University, Materials theory group. I appreciate the enthusiastic support of all co-workers from these departments, as well as many discussions with colleagues from the Institute of Physics.

I would like to thank in particular my collaborators from Prague Pavel Baláž, David Wagenknecht, Jakub Šebesta, Martin Žonda, Josef Kudrnovský, Václav Drchal, František Máca, Martin Diviš, and my former supervisor Ilja Turek. I also appreciated work with Dominik Legut from Ostrava, my collaborators from Uppsala Peter M. Oppeneer, Pablo Maldonado, Marco Berrita, Marco Battiato, Johan Hellsvik, Ritwik Mondal, and all others who contributed to my understanding of problems that we are trying to solve.

Last but not least I would like to thank my wife Hana and my whole family for their support and patience during my scientific carreer.

Chapter 1

Introduction

Mankind has been aware of magnetism already since the times of ancient Greeks, who provided the first description of magnetite properties. Its first significant application, a compass, has been constructed more than two thousand years ago in ancient China. However, proper understanding of magnetism became possible as late as in 20th century. Magnetization as a source of permanent magnetic field is connected with angular momentum of electrons, but in classical mechanics it is hard to imagine that a nonzero, stable angular momentum is present even at lowest energy. On the other hand it is known that permanent magnetization is generally highest at lowest temperatures. Quantum mechanics resolves this problem by showing that electrons can possess finite angular momentum at the lowest energy level, therefore magnetization can be present at ground state. Moreover it introduces spin as an internal angular momentum of electron without any classical analogue, and this momentum is in fact often more important than the orbital motion related electronic angular momentum. Magnetism can obviously be understood only with quantum mechanics, and relativistic effects also turn out to be important in many cases.

In this work I concentrate on microscopic understanding of various effects related to magnetism. While a description of magnetism can be provided by micromagnetism, a method relevant especially for problems on a larger scale like domain walls, the most current problems require a deeper approach that is provided by atomistic spin modeling [1, 2]. Great advances in computational methods, in particular the density functional theory [3, 4], have made it possible to describe magnetism on a quantitative level from first principles [5, 6], thus avoiding any free parameters as much as possible.

Advanced methods allow us to discover magnetic momentum on individual atoms. The relation between macroscopic magnetization and local microscopic moments is generally not trivial: For example, a system with nonzero local moments may still have zero total moment (and at least two different kinds of magnetic order correspond to that: the paramagnetic one and the antiferromagnetic one). Ordering of local moments thus represents a crucial question and its evaluation rests on the knowledge of the interaction between moments on different atoms. Notably, this interaction is again predominantly of quantum mechanical origin, based on the Pauli exclusion principle. The dipole interaction becomes important only on longer scales. Finding the magnetic order under different conditions is thus one of the main tasks for a theory describing magnetism, and a full description including finite temperature effects and external influences requires to incorporate quite complex methods. Some of the most important methods involved here, basically prerequisites for our further research, are described in Chap. 2.

Magnetic properties depend significantly on temperature. Understanding finite temperature magnetism (including of course room temperature behavior) requires to describe the competition between internal exchange interaction and thermal fluctuations. Magnetization dynamics is ideally suited for this task. Our work related to this equilibrium problem is described in Chap. 3. One specific subproblem of this kind is a question of a stability of magnetic direction of a homogeneously magnetized grain against thermal fluctuations. Note that such magnetization direction represents an information that can be easily read by technical devices and can thus be used for data storage. For long time stability of stored information it is needed that there exists an energy barrier separating possible states of magnetic system. This barrier arises due to magnetocrystalline or shape anisotropy. Our results regarding magnetocrystalline anisotropy are presented here as well.

Even more appealing questions are related to magnetization changing in time, which can also mean controlled manipulation of magnetization. That basically means writing an information in the sense described above, and it is a problem of high importance for the novel field of spintronics. Industry and society has a need to increase the density of information carried by magnetic storage media together with the speeding up of the reading and writing processes. This topic also contains many points interesting from the scientific point of view, as we show later. Subsequent chapters are thus devoted to non-equilibrium problems, and concentrate on most recent novel methods to manipulate magnetization that I have studied: by means of electrical current (Chap. 4) and due to an action of femtosecond laser (Chap. 5).

The femtosecond timescale in magnetization dynamics represents a source of a lot novel information on physics of magnetism and introduces the possibility to examine magnetic systems far from equilibrium. The widely debated effect of ultrafast demagnetization [7] is related to the connection between magnetism and angular momentum mentioned in the beginning: demagnetization requires transfer of angular momentum from the magnetic subsystem to other degrees of freedom, and on a fs timescale this process can be closely examined. The connection to the angular momentum has been studied already in the Einstein-de Haas experiment, where the change of angular momentum due to the loss of magnetization has been seen to be compensated by an increase of macroscopic angular momentum [8]. Understanding microscopic mechanism of this transfer represents one of the main problems of ultrafast demagnetization, one can for example speculate how much it is linked to the effect that Einstein and de Haas has observed. The ongoing research in this field has already led to many interesting discoveries [9], e.g. formation of a state where the ground state magnetic order is reverted for a short time, e.g. the antiferromagnetic ordering into ferromagnetic [10], or an increase of the magnetization above its ground state value [11]. However, many observations lack complete explanation and there is thus a lot of space for theoretical investigations. We have attempted to shed more light on some open problems in this work.

Chapter 2

Basic concepts

The first step in the development of atomistic modeling of magnetism represents the Ising model introduced in 1925 [12]. Despite its simplicity it still finds applications especially to describe phase transitions, even outside the field of physics.

One can also look at the problem from a different perspective and attempt to construct the most accurate quantum model of a magnetic material from first-principles [13], based on the density functional theory (DFT). Notably, microscopic origin of magnetism rests on various underlying exchange interaction mechanisms between electrons, and represents generally a complicated many-body problem. The time-dependent density functional theory would be even more suitable for magnetism studied on the ultrafast timescale, there are however numerous obstacles to be solved when this method is applied to magnetization dynamics [14–17]. These approaches are overall numerically very demanding and the size of a possible employed simulation cell is limited. On the other hand, in reality large spatial correlations or the inclusion of finite temperature effects may be needed, and this requires a large cell.

2.1 Construction of atomistic model

Therefore, a more efficient multiscale approach to describe magnetization dynamics has been proposed [18–20]. This method incorporates information from quantum mechanical solution, while allowing to solve very large systems. It rests on mapping the magnetic part of the full electronic Hamiltonian onto an atomistic model based on the Heisenberg Hamiltonian (HH), essentially an Ising model where atomic magnetic moment direction can change in 3D space [21]. This Hamiltonian is given as

$$\mathcal{H} = -\frac{1}{2} \sum_{i,j} J_{ij} \, \boldsymbol{S}_i \cdot \boldsymbol{S}_j - \sum_i \boldsymbol{H}_i \cdot \boldsymbol{S}_i \,, \tag{2.1}$$

where a classical moment $\boldsymbol{S}_i$ is assigned to each atom, $\boldsymbol{H}_i$ is the local effective magnetic field encountered by i-th moment. Field $\boldsymbol{H}$ may include not only an external field but also effective magnetic fields due to the magnetocrystalline anisotropy. Inclusion of other effects is discussed later in the text. J_{ij} describes the exchange interaction between the i-th and j-th spins.

All parameters of the Heisenberg Hamiltonian, i.e. magnitudes of spin moments S_i and exchange constants J_{ij}, can be provided by first principles calculations [2]. Details of electronic

structure calculation methods go beyond the scope of this text and while their knowledge is important for understanding some construction shown here, we refer the reader to existing literature on this subject [20, 22]. Within the standard approach to solving HH the variation of these parameters is usually considered negligible, and only the directions of spin moments $\boldsymbol{S}_i$ are allowed to change. Possible shortcomings of this approximation are discussed in Sec. 2.2. Additionally, the assumption of classical moments makes it impossible to describe correctly low temperatures, where quantum behavior dominates and is responsible for example for the Bloch $T^{3/2}$ law. Nevertheless, the dynamics of the mapped spin system is still a difficult, multidimensional problem, which has to be solved numerically.

As long as the spin wave energy is much smaller than the bandwidth and the exchange splitting [23] the assignment of the energy of a system with perturbed magnetic moments direction to the exchange constants J_{ij} in the HH, Eq. (2.1), is highly accurate. This limit corresponds to the limit of infinitesimally small momentum tilting.

The energy of such a tilted magnetic configuration can be calculated using the constrained DFT method, where the magnetic moment directions are possible constraints enforced by means of Lagrange multipliers. One method to calculate exchange interaction J_{ij} is thus to generate a magnetic configuration based on a spin wave with wavevector $\mathbf{q}$ (frozen-magnon method) and calculate its total energy $E(\mathbf{q})$. The knowledge of this energy for more different wave vectors allows to extract J_{ij}, the number of needed $E(\mathbf{q}_n)$ depends on the number of nearest neighbor shells where J_{ij} is non-negligible.

Alternatively it is possible to utilize the magnetic force theorem. The theorem states that changes of the energy due to infinitesimally tilted individual spin quantization axis correspond to changes of one-particle energy eigenvalues for a system where the ground state magnetization is modified by this tilting non-selfconsistently. Therefore there is no need for multiple DFT calculations converging to self-consistency and the method is highly efficient. Application of this theorem leads to the Lichtenstein formula [18]. This allows to obtain J_{ij} directly from the knowledge of spin-dependent Green functions G^σ and the magnetic field from the exchange-correlation potential $B_{xc}(\mathbf{r}) = V^\uparrow(\mathbf{r}) - V^\downarrow(\mathbf{r})$:

$$J_{ij} = \frac{1}{\pi}\text{Im} \int_{-\infty}^{E_\text{F}} \text{d}E \int_{\Omega_i} \text{d}\mathbf{r} \int_{\Omega_j} \text{d}\mathbf{r}' B_{xc}(\mathbf{r}) G^\uparrow(\mathbf{r}, \mathbf{r}', E^+) B_{xc}(\mathbf{r}') \bar{G}^\downarrow(\mathbf{r}', \mathbf{r}, E^-) \qquad (2.2)$$

where $\sigma = \uparrow, \downarrow$ is the spin index, Ω_i is volume of sphere with center in i-th atom position, E_F denotes the Fermi energy, and $E^+ = \lim_{\alpha \to 0} E + i\alpha$ [23].

Another component of the Heisenberg model is the local magnetic momentum magnitude. Local spin and orbital moments m_S, m_L correspond to mean values of operators S_z and L_z. With the knowledge of the spin-resolved density of states (DOS) $n^\sigma(E)$ the spin momentum can conveniently be obtained from $m_S = \mu_B \int_{-\infty}^{E_F} [n^\uparrow(E) - n^\downarrow(E)]\,\text{d}E$. Non-zero orbital momentum is obtained in bulk solids when spin-orbit (SO) interaction is present. Notably, in transition metals it is strongly suppressed by crystal field, while in rare earth metals it can reach values higher than the spin momentum. Orbital momentum contributes in a similar way as spin momentum to the interaction with an external field, but its behavior differs fundamentally from spin momentum in many other aspects. In all problems studied here the orbital momentum can be neglected and we thus put $|\boldsymbol{S}_i|$ equal to m_S corresponding to the i-th particular atom. The local spin momentum is generally affected by the surrounding environment. For example it is known to grow with decreasing number of neighbors - at a surface, in a cluster or at atomic wires many atoms of bulk nonmagnets become magnetic. It

is also strongly affected by deformation, and in both these cases first principles calculations can provide invaluable predictions of its behavior [24, 25]. It would also be influenced by alloying with another metal, or by temperature as described below. However, the dominant contribution to finite temperature magnetization $M(T)$ are transversal excitations that do not change the momentum magnitude. Therefore it is possible to neglect changes in local momentum magnitudes with temperature within the effective Heisenberg model. This approach has been successful in describing finite temperature properties of many ferromagnets, and provides an accurate description even for systems with predominantly itinerant electrons, as demonstrated for magnon spectra and $M(T)$ in Fe, Co and Ni [19]. Nevertheless, one should be aware of the approximate character of mapping magnetic problems to HH. For example it neglects the presence of Stoner excitations, whose contribution has recently been calculated from time-dependent density functional theory [26].

2.2 Disordered local moment method

There are effects that go beyond the assumptions of temperature independent exchange constants and moments in the Heisenberg Hamiltonian, especially at higher temperatures. Such effects can be described by including the temperature induced change of magnetic order in the ab initio calculation of parameters entering HH. Examination of the effect of individual magnetic excitations - magnons - is not necessary at high enough temperatures, since several different magnons affect each site and their effect can therefore be averaged. The disordered local moment (DLM) method assumes each site to have a random deviation from the ferromagnetic (FM) order with its average magnetization equivalent to that of the system with magnons. It has been shown to provide a good description of finite temperature magnetism [27] and it can also provide framework to calculate other properties affected by magnetization decrease, as is the resistivity [28]. The situation with complete disorder, corresponding to zero average magnetization, is in turn applied to the paramagnetic state. One can also define a partial magnetic disorder (partial DLM), whose average magnetization is linked to a particular temperature T so that it is reduced as compared to the ground state according to the sample $M(T)$ curve. When employing the DLM method the electronic structure can in fact achieve selfconsistency at the state of magnetic disorder induced by finite temperatures. The exchange interaction and local momentum for the given temperature employed in HH can thus be adjusted and the accuracy of the atomistic model increased. Note that local moments often change only slightly with magnetic disorder [22], which partially justifies the general application of Heisenberg model, but features in the density of states are smeared out and change of exchange constants can be significant. In this manner even critical temperatures can generally predicted with a higher accuracy considering exchange constants from the full DLM state very close to the situation at a critical temperature rather than those from the ground state. Note that exchange interactions can become modified by various different influences and in the context of femtosecond magnetism also due to rapid changes of electronic temperature [14, 29].

A reasonably accurate description is provided even when the noncollinear magnetic disorder is replaced by an alloy composed of only two oppositely oriented spin orientations given as $X^{\uparrow}_{(1+r)/2}X^{\downarrow}_{(1-r)/2}$, where r is an auxiliary order parameter ($0 \leq r \leq 1$). Magnetic moments are fully ordered for $r = 1$, completely disordered for $r = 0$, and the states between correspond to the Landau-Lifshitz-Gilbert partial (uncompensated) DLM. The introduced disorder can be
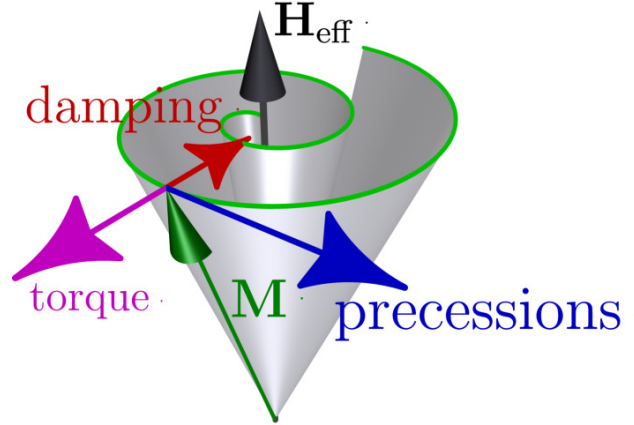
Figure 2.1: Different contributions to the evolution of a magnetic moment

described by the coherent potential approximation [30]. This method has for example been applied to study finite temperature properties of dilute magnetic semiconductors [31]. Local moment disorder can also be modeled employing quasi-random supercells, which allows to also include various correlations and other complex effects. Such approach has recently led to surprising findings concerning the discrepancy between predicted and calculated moments in Fe_2AlTi [32].

2.3 Spin dynamics

The dynamics of magnetic moment can be decomposed into three contributions: precession around an effective field, magnetic relaxation due to energy dissipation of a precessing magnetic moment, and a torque due to various external influences (Fig. 2.1). While the precession is a simple consequence of quantum mechanics principles, the relaxation (damping) is given by complex processes. It has been intensively studied since its introduction [33], and scales with the Gilbert damping parameter α_G [34]. For more information about its theoretical description we refer the reader to the vast literature on this interesting subject [35–38]. Existence of the third term, the torque, is a precondition for manipulation of magnetization. Most of the problems studied in Chapters 4 and 5 thus correspond to an evaluation of the torque term in a specific situation, e.g. spin-transfer torque. This evolution can be described by the Landau-Lifshitz (LL) equation, shown here together with a general torque term $\boldsymbol{\tau}$:

$$\frac{d\boldsymbol{S}_i}{dt} = -\gamma \boldsymbol{S}_i \times \boldsymbol{H}_i - \gamma \frac{\alpha_G}{S_i} \boldsymbol{S}_i \times (\boldsymbol{S}_i \times \boldsymbol{H}_i) + \boldsymbol{\tau} \, . \tag{2.3}$$

Here $\gamma = g\mu_B/\hbar$ is the gyromagnetic ratio. This equation can be recast into the more commonly used Landau-Lifshitz-Gilbert (LLG) equation, where spin momentum in the relaxation term is replaced by its time derivative, which leads to the renormalization of γ [2, 34].

At finite temperatures magnetization is affected by a number of random microscopic scattering events on the time scale far shorter than the one of magnetization dynamics. These can be incorporated into LLG equation in terms of Langevin dynamics by adding a stochastically fluctuating field, $\boldsymbol{\xi}$ to the effective field as formulated by W. F. Brown [39]:
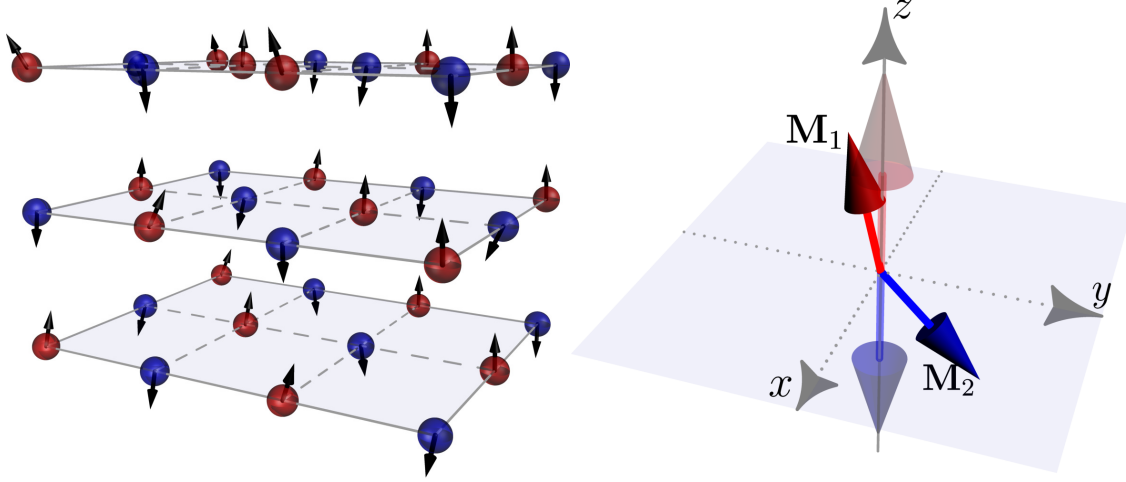
Figure 2.2: Different approaches to magnetization dynamics: atomistic and macrospin dynamics, shown for a system with two magnetic sublattices.

$\boldsymbol{H} \to \boldsymbol{H} + \boldsymbol{\xi}$. The fluctuating field must follow statistical conditions for a Gaussian process with zero mean, thus for the components $\boldsymbol{\xi}_i(t)$ one can can write

$$\langle \boldsymbol{\xi}_i(t) \rangle = 0 \,, \tag{2.4a}$$

$$\langle \boldsymbol{\xi}_i(t) \boldsymbol{\xi}_j(t') \rangle = 2 \, \mathcal{D} \, \delta_{ij} \delta(t - t') \tag{2.4b}$$

where $\langle \ldots \rangle$ is the time average. Then the thermal equilibrium distribution of the average magnetization in an effective field should be of Boltzmann type, which is most easily verified for single spin [1]. The variance of thermal field components is directly related to the temperature and damping, in agreement with the fluctuation-dissipation theorem [40]: $\mathcal{D} \propto \alpha_G \, k_B T$, where k_B is the Boltzmann constant. In the works presented here we used Uppsala Atomistic Spin Dynamics (UppASD) code [2, 41, 42].

Magnetic configuration on the atomistic level is reflected in the macrospin, $\boldsymbol{M} = \langle \boldsymbol{S} \rangle$ (Fig. 2.2). For example, increasing thermal disorder of atomistic moments leads to a reduction of the macrospin. An alternative approach to magnetization dynamics based on direct application to the macrospin has been proposed [43]. In this case the relaxation part of the magnetization dynamics consist of two parts $\boldsymbol{\tau}_{\text{rel}} = \boldsymbol{\tau}_\perp + \boldsymbol{\tau}_\parallel$, where $\boldsymbol{\tau}_\perp$ is the transverse relaxation term, which is analogical to Gilbert of Landau-Lifshitz damping term, and $\boldsymbol{\tau}_\parallel$ is the longitudinal relaxation term. These are given as follows:

$$\boldsymbol{\tau}_\perp \propto \alpha_\perp \, \boldsymbol{M} \times [\boldsymbol{M} \times (\boldsymbol{H} + \boldsymbol{\xi}_\perp)] \,, \tag{2.5a}$$

$$\boldsymbol{\tau}_\parallel \propto \alpha_\parallel \, \boldsymbol{M} \, (\boldsymbol{M} \cdot \boldsymbol{H}) + \boldsymbol{\xi}_\parallel \,. \tag{2.5b}$$

Here dimensionless $\alpha_\perp$ and $\alpha_\parallel$ are transverse and longitudinal damping parameters, respectively. The resulting dynamical equation describing macrospin evolution is called the Landau-Lifshitz-Bloch equation (LLB). We have applied this method to study laser-induced magnetization dynamics of sublattices of a ferromagnetic alloy, Permalloy (Py = $Fe_{20}Ni_{80}$), where a generalization of this method to multi sublattice systems was needed [A.1].

2.4 Magnetocrystalline anisotropy

An important contribution to the effective magnetic field $\boldsymbol{H}$ represents magnetocrystalline anisotropy, since it affects thermal stability of selected magnetization orientation. A prerequisite for its presence is the spin-orbit (SO) interaction which connects orbital momentum originating from lattice with spin momentum, the main contribution to magnetization. A high magnetic anisotropy energy (MAE) is beneficial for data storage applications. Furthermore, in thin layers a higher miniaturization of data units can be achieved with the preference for perpendicular-to-plane orientation. This is however more difficult to achieve since the shape anisotropy always prefers in-plane orientation, and magnetocrystalline anisotropy has to overcome it. Note that later in the text we always refer under the term MAE to the shape independent magnetocrystalline contribution. Often MAE is very small (less than mRy per atom), but still it has important consequences for material properties. This small value represents a challenge for first principles quantum theory methods [44]. Nevertheless, these methods may be successful in determining this quantity, but use of all approximations affecting even slightly features near the Fermi level have to be carefully examined [45]. Note that due to its significant anisotropy even antiferromagnetic (AFM) systems can be used as a spintronics memory device [46, 47]. There is a number of interesting findings regarding magnetic anisotropy of more exotic systems, for example iron adatoms forming Hund's impurity [48].

We have calculated MAE for $Fe_{1-x}Co_x$ alloys, well known for a high spontaneous magnetization. Furthermore, their deposition on various substrates allows to perform tetragonal deformation, forming the so called body-centered-tetragonal (bct) $Fe_{1-x}Co_x$ alloys along constant volume Bain path. Such a general sctructure can be characterized by its c/a ration, whose specific value $c/a = 1$ corresponds to the bcc lattice, while $c/a = \sqrt{2}$ represents the fcc lattice.

In this case an uniaxial MAE is present, described by $K_u = E^{(100)} - E^{(001)}$, where $E^{(\alpha\beta\gamma)}$ is the total energy for a system with magnetization aligned along the $(\alpha\beta\gamma)$ direction. Previously, a large MAE (up to 0.8 meV/atom) preferring perpendicular alignment has been predicted, employing the virtual crystal approximation (VCA) [49]. However, in experiments MAE has been enhanced for specific substrates [50, 51] enough to overcome the shape anisotropy, but reported values are significantly smaller than predicted by theory. We have performed calculations of MAE employing the coherent potential approximation (CPA) [30], and obtained MAE as a function of both the c/a ratio and the Co concentration x (Fig. 2.3) [A.2].

Our calculations allow us to conclude about the accuracy of disorder treatment methods here: with a simple treatment by means of the VCA the MAE is overestimated as compared to the more accurate CPA method. Apparently the disorder smears out eigenstates near the Fermi level in the minority-spin channel, which leads to the reduction of MAE. On the other hand, the use of local spin density approximation (LSDA) as the exchange-correlation potential leads to underestimation of MAE. We also show that a significant difference occurs between calculations employing the fully relativistic Dirac (FRD) equation and calculations employing only the first order relativistic corrections to the scalar relativistic approximation (SRA) including the spin-orbit interaction (Fig. 2.4). A correlation between MAE and the anisotropy of magnetic moment has been found in cases when the SO interaction is weak as compared to the exchange splitting and the bandwidth [52]. Our calculations have verified
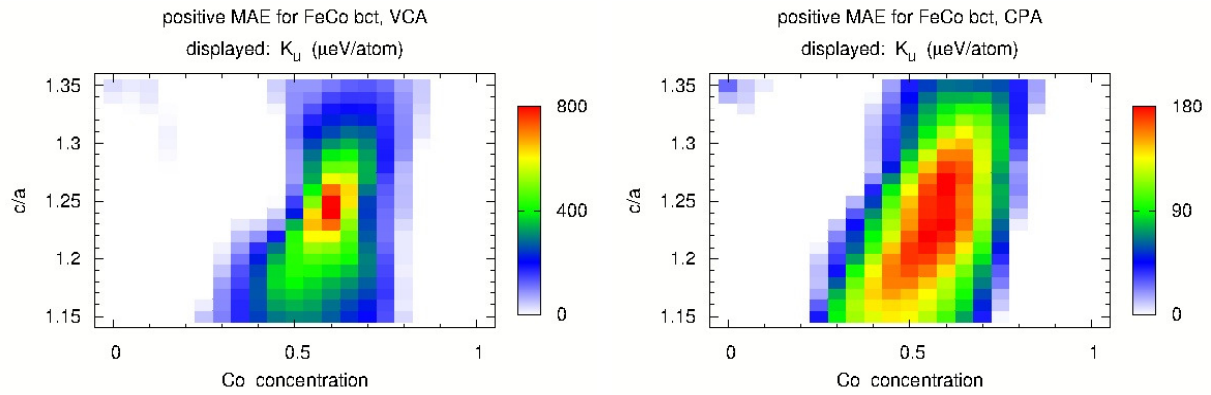
Figure 2.3: The uniaxial MAE of random bct $Fe_{1-x}Co_x$ alloys as a function of the Co concentration and of the tetragonal strain c/a: calculated in the VCA (a) and in the CPA (b). Only positive values of the K_u are displayed in both plots; the corresponding colored scales are in μeV/atom [A.2].

the existence of this correlation also for $Fe_{1-x}Co_x$ alloys [A.3]. Recently, extra doping with carbon has been found to increase MAE even more, opening the way for replacement of permanent rare-earth based magnets by $Fe-Co-C$ alloys and thin films [53]. In another promising permanent magnet replacement, Fe_5PB_2, alloying with Co has led to a decrease of MAE [54], contrary to its effect in Fe alloys.
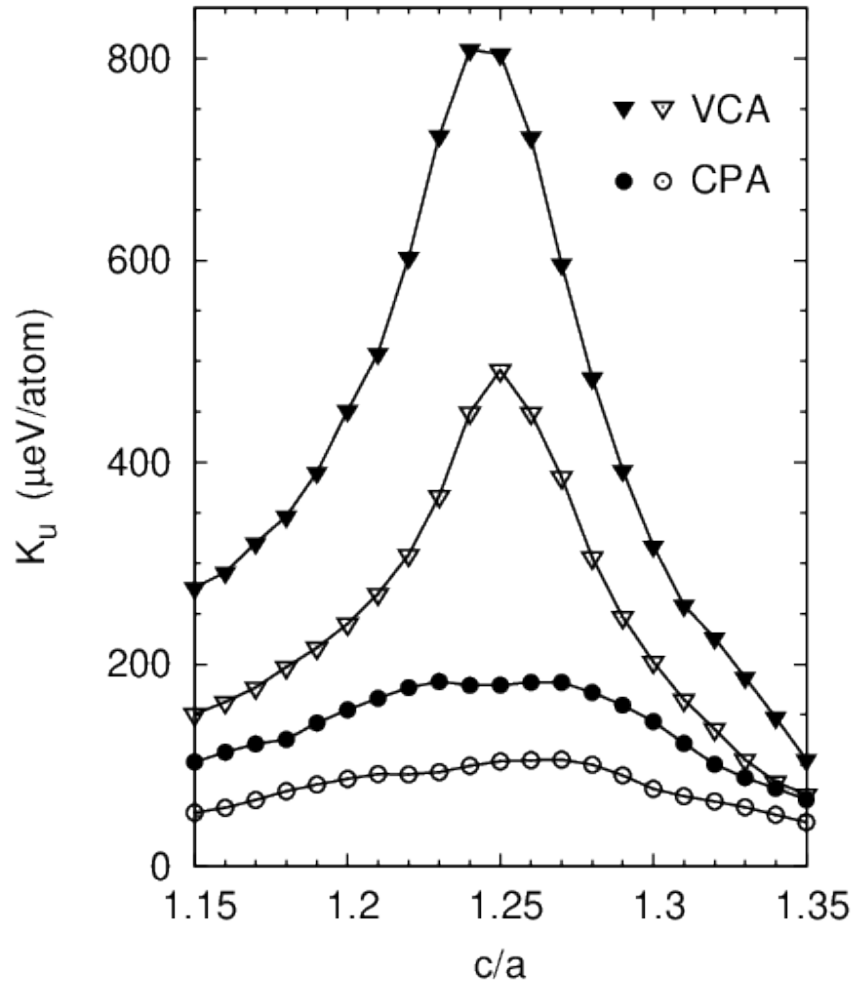
Figure 2.4: The uniaxial MAE of the bct $Fe_{0.4}Co_{0.6}$ alloy as a function of the c/a-ratio, calculated in different approximations (VCA – triangles, CPA – circles) and approaches: FRD – full symbols, SRA+SO – open symbols [A.3].

Chapter 3

Magnetization dynamics in equilibrium

Here we concentrate mainly on the study of temperature-dependence of magnetization, without any external driving field that could cause time-dependence of macroscopic magnetization, hence a steady state. Concerning the class of equilibrium problems, we should note that even finding the ground state magnetic order can represent a challenging task, for example for the cases of dilute or frustrated systems [55]. However, their description can often benefit from the same statistical apparatus developed for finite temperature problems, so the ground state can be obtained simply by considering the $T \to 0$ K limit after a proper application of the methods described below.

Stochastic effects due to finite temperature can be described by Langevin dynamics (Sec. 2.3). However, for magnetization dynamics without time dependence it is often sufficient to employ Monte Carlo (MC) Metropolis algorithm [1, 56], recast into a form more efficient for spin dynamics [57]. Simulations are then usually started from a paramagnetic state at sufficiently high temperature. During simulations the temperature is continually decreased with a small step towards $T = 0$. At each temperature step a sufficient number of MC steps has to be performed (10^5 up to 5×10^5 in our simulations). To improve the statistics more identical systems are simulated in parallel and the contributions of all of them averaged. This can benefit a lot from parallel execution utilizing more computational nodes.

Spin dynamics can be used to find critical temperatures T_C corresponding to changes of magnetic ordering, i.e. Curie temperatures for FM systems, or Néel temperatures for AFM systems. While such transition is most naturally observed in the $M(T)$ curve, at T_C also a peak of susceptibility and specific heat appears. This typically allows to determine T_C with a higher accuracy than from the $M(T)$ curve because of a finite size of the simulation cell and other numerical limitations. An even more accurate method utilizes Binder cumulants defined as

$$U \equiv U(L,T) = 1 - \frac{\langle M^4(L,T) \rangle}{3 \langle M^2(L,T) \rangle}, \tag{3.1}$$

where $\langle \dots \rangle$ stands for averaging over MC steps at a constant temperature. Plots of $U(L,T)$ vs. temperature calculated for different sizes L intersect at $T = T_{\mathrm{C}}$ [58]. Nevertheless, any of these approaches predicts T_C with a higher accuracy than the mean field theory, while computational requirements remain acceptable.
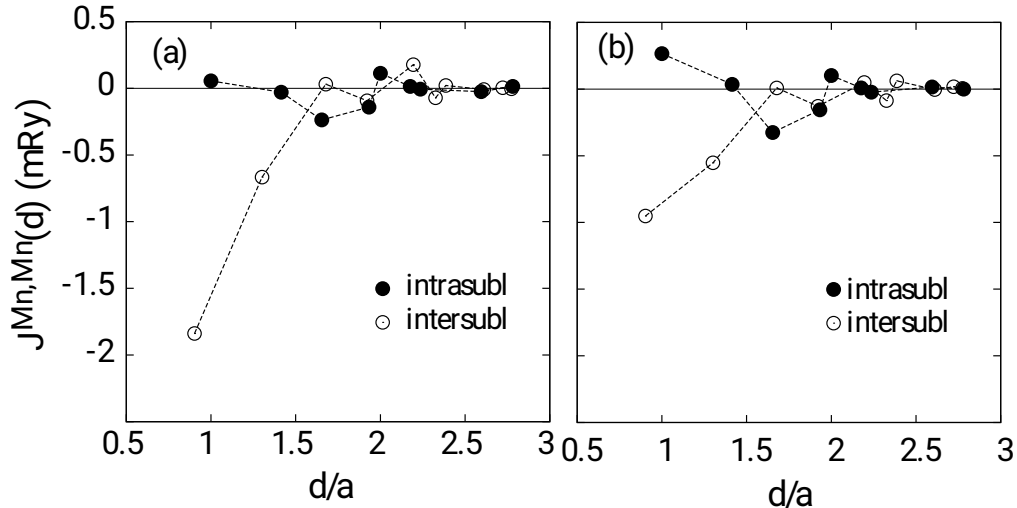
Figure 3.1: Exchange integrals for the tetragonal CuMnAs between Mn-atoms as a function of the distance d (in units of the lattice constant a): (a) The phase I, AFM state, (b) the phase I, paramagnetic (DLM) state, and (c) the phase II, DLM state [A.4]. The exchange interactions are subdivided into two groups, namely, between Mn-atoms on the same sublattice (solid circles) and between atoms on different sublattices (open circles).

3.1 Application to an antiferromagnet

Magnetization dynamics in antiferromagnets has many unique features, let us name for example the recent discovery of multiple stable configurations for switching here [59, 60]. We have used the above described methods to study magnetization in antiferromagnetic CuMnAs, system interesting for several reasons. In its tetragonal phase (space group P4/nmm) it is a half-metal, and a manipulation of its magnetization by spin-orbit torques has recently been demonstrated [61], together with the mentioned multiple stability. Notably, ideal bulk samples prefer orthorhombic structure, but the tetragonal phase can be stabilized in epitaxial samples or by non-ideal stoichiometry, especially with excess Cu [62]. X-ray measurements indicate that epitaxial samples were also Cu rich [63], hence all tetragonal samples most probably contain significant amount of defects.

We have calculated the electronic structure system by means of both the linear muffin-tin orbital (LMTO) method [22] and the pseudopotential method based on the full-potential Vienna ab-initio simulation package [64]. The first method is well suited for the application of the CPA method and exchange interaction calculation, but its accuracy may be lower than that of the latter one. We have evaluated the formation energy of several different defects that can occur in the system and analyzed how much they can contribute to the experimentally observed quantities [A.4], employing 48 atoms $Cu_{16}Mn_{16}As_{16}$ in VASP. We have confirmed that Mn_{Cu} and Cu_{Mn}antisites are the most probable defects here [A.5]. For the first time we have calculated exchange interactions (Fig. 3.1) in this system from the Lichtenstein formula, Eq. (2.2). Note the significant difference of interactions between those derived from the ground state (AFM state), and from the approximated paramagnetic state (the DLM state). The latter is on average smaller in absolute value than the the former.

Spin dynamics has been employed to obtain the $M(T)$ curve for individual sublattices (Fig. 3.2). Note that sublattice magnetizations cancel each other in the simulation, as it is
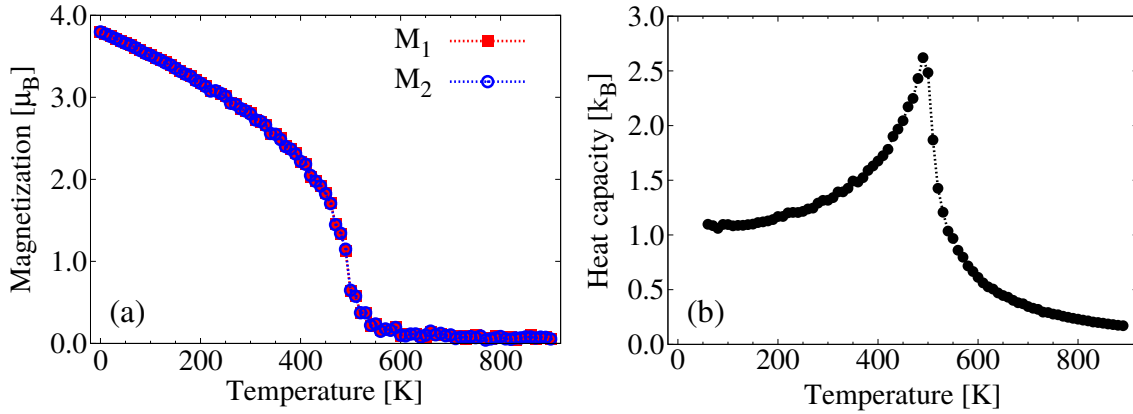
Figure 3.2: (a) Magnetizations of the Mn-sublattices as a function of temperature assuming exchange integrals derived from the paramagnetic (DLM) state of the tetragonal CuMnAs with the phase I structure. By symmetry, the dependence of both sublattice magnetizations on the temperature is the same. (b) The temperature dependence of the heat capacity from which the Néel temperature can be extracted more accurately (about 480 K) [A.4].

expected for an antiferromagnet, and because of that it does not make sense to study the total magnetization. This method provides the Néel temperature with a lower precision, we extract it more accurately from the specific heat (Fig. 3.2). The calculated interactions lead to the Néel temperature $T_N = 680$ K if derived from the exchange interactions in the AFM state. The more accurate approach starting from the DLM state provides $T_N = 480$ K [A.4], which is actually in a very good agreement with the experimental result of 507 K for the most ideal sample [62].

3.2 Application to topological insulators doped by magnetic atoms

Topological insulators (TI) exhibit highly interesting transport features, for example the interesting spin structure of its surface states may allow optical control of spin currents [65]. The description of this class of materials goes beyond the scope of this work and can be found in a comprehensive review [66]. We shall discuss here only properties relevant to the problem studied. The surface state in topological insulators is protected against perturbations that keep time-reversal symmetry. Magnetic order violates time-reversal symmetry and thus may affect largely transport properties of topological insulators connected with the forbidden backscattering. Magnetic doping then provides a way to add novel functionality to topological insulators [67], as well as a test of stability of topological properties. It is needed to distinguish the cases with and without long range magnetic ordering to see whether time reversal symmetry is broken. Some studies already challenge the present understanding here and suggest that gap opening is not related to ferromagnetic order [68], which renders finding the real consequences of magnetic doping even more important. Spin dynamics methods discussed in this chapter can provide information in what situations can magnetic order be expected and help to understand other of the many open questions in this field.

Magnetic doping of TI represents here a problem from the class of dilute magnetic systems. Furthermore, the problem is complicated by the fact that Mn can occupy different positions
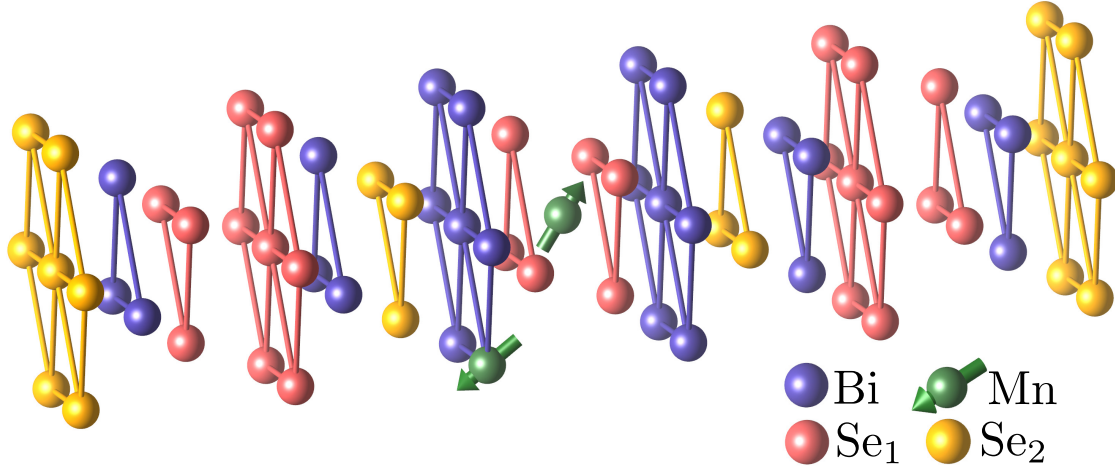
Figure 3.3: Bi_2Se_3 crystal structure, a hexagonal supercell. Possible Mn dopant positions, namely the substitutional one (Mn_{Bi}) and the interstitial one in the van der Waals gap (Mn_i) are indicated. Note the two nonequivalent Se positions.

in the lattice (Fig. 3.3), and these lead to generally different magnetic interaction between them. In order to understand this we have used the linear muffin-tin orbital (LMTO) method [22] to calculate the electronic structure of Bi_2Te_3 and Bi_2Se_3 doped by Mn at different possible positions in the lattice and also in the presence of antisites and vacancies. This provides for the first time a comprehensive map of possible behavior affecting strongly the bulk resistivity, carrier concentration and magnetism [A.6]. Density of states calculations reveal in which case the Fermi level lies at low conducting impurity Mn peak, and which effects shift it. This allows us to tune the bulk resistivity, and also help to uncover the location of Mn atoms. Concentration dependence of resistivity exhibits significant difference between the substitutional Mn_{Bi} or interstitial Mn_i position. According to calculations the observed behavior does not correspond to a presence of only one type of defect or impurity, especially the inclusion of interstitials in addition to the substitutional Mn_{Bi} might explain existing discrepancies [A.6].

In some experiments Mn dopants embedded in Bi_2Se_3 ordered ferromagnetically [68–70], in some it remained paramagnetic [71]. In other to understand this, exchange interactions between Mn magnetic moments in bulk Mn-doped Bi_2Te_3 and Bi_2Se_3 have been calculated using ab initio methods. For Mn in the substitutional Mn_{Bi} position we have found that E_F lies in the impurity peak causing higher resistivity, and positive and negative interactions are relatively balanced. This can be interpreted as a competition between negative superexchange-like interaction vs. mostly positive carrier-mediated interaction For Mn in the interstitial Mn_i position there is a higher contribution of p-states at E_F, thus a lower resistivity. We see a strong J_{ij} decay in the z direction, exchange between QL is thus much smaller than inside it (Fig. 3.4).

Employing the calculated exchange constants we have systematically studied ferromagnetic Curie temperatures and other magnetic magnetic properties by means of atomistic MC simulations. We find that the ferromagnetic ordering is possible for some configurations, and link the tendency to it to the Fermi level position. Curie temperatures are shown to be significantly dependent on the concentration of Mn atoms in substitutional and interstitial positions (Fig. 3.5 for Bi_2Se_3). When more defects are combined, the most important point
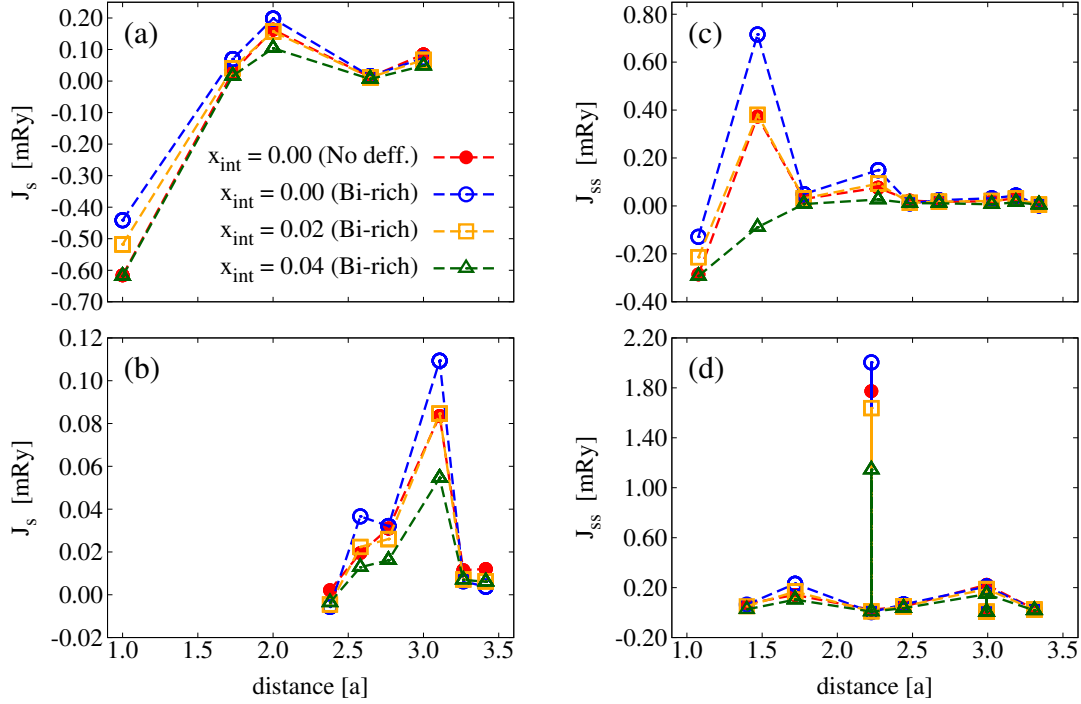
Figure 3.4: Exchange interactions between magnetic moments of substitutional Mn_{Bi} atoms embedded in Bi_2Se_3: (a) moments belonging to the same Mn_{Bi} sublattice of the same QL, (b) moments belonging to the same Mn_{Bi} sublattice in neighboring QLs, (c) moments belonging to different Mn_{Bi} sublattices of the same QL, (d) moments belonging to different Mn_{Bi} sublattices in neighboring QLs. The solid dots mark the interactions in case of no native defects and no interstitial Mn atoms ($x_{int} = 0.00$). The oped symbols marks interactions with Bi_{Se} native defects (Bi-rich form) for different concentrations of interstitial Mn_i atoms: $x_{int} = 0.00$ (dots), $x_{int} = 0.02$ (squares), $x_{int} = 0.04$ (triangles).

is the final position of E_F. FM order is actually predicted for most $p-$type samples. For border cases the ground state appears to be not completely ferromagnetic, but canted. Within the range that can be achieved by defect concentrations up to 10% we see that the lower is E_F, the higher is T_C. From this it follows that the addition of Mn_{Bi} raises T_C, while other considered defects lower T_C (Mn_i and V_{Se} vacancies). However, addition of too much Mn_{Bi} has not led to the expected increase of T_C in experiments, which may be caused by inevitable formation of other unwanted defects. An efficient way to shift E_F to the valence band could be doping with extra nonmagnetic dopants that are known to lower the Fermi level.

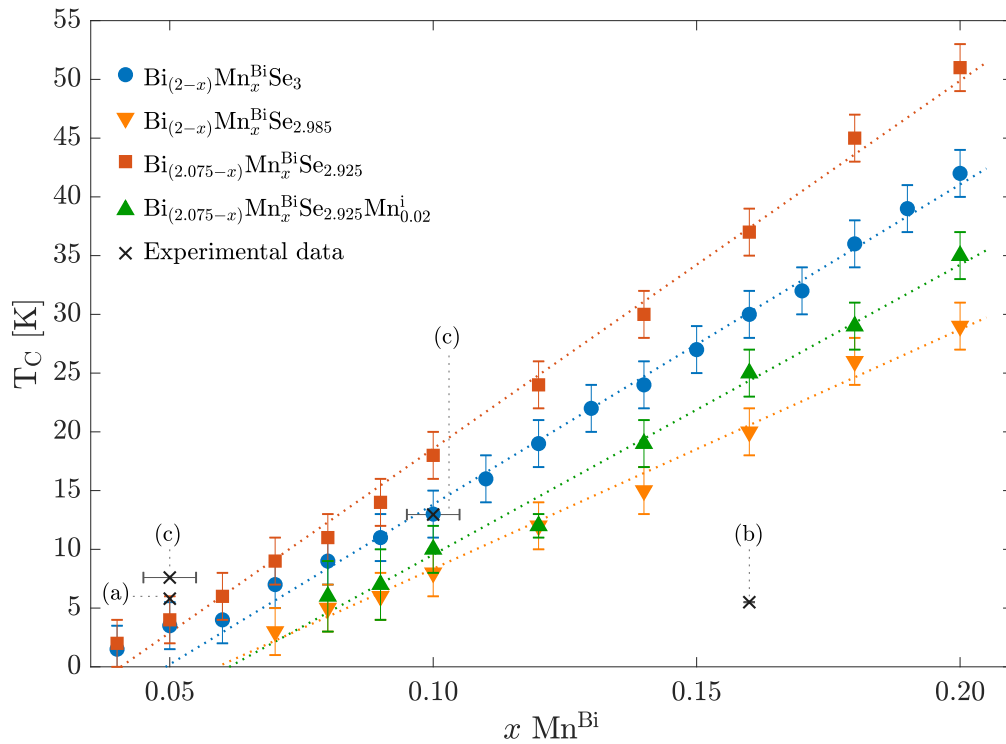Figure 3.5: Dependence of the Curie temperature on concentration of the substitutional Mn_{Bi} atoms per f.u. x and fits to the calculated points. Depicted data: (blue) Mn_{Bi} defects only, (red) Mn_{Bi} and Bi_{Se} defects, (green) previous case together with Mn_i, (orange) Mn_{Bi} defects with V_{Se}, (gray) experimental data - multilayers: (a)[69], (b) [68] (bulk single crystal) (c) [70] .

Chapter 4

Magnetization dynamics induced by current

Charge current can affect magnetization indirectly, for example via heating. Furthermore, it can also be spin-polarized, and thus give rise to a spin current (SC). A crucial property of spin current is the ability to exert torque on a magnetic system, and thus induce dynamics and possibly also revert magnetization into another stable state (current induced magnetization switching) [72]. This so-called spin-transfer torque (STT) is always originating from the spin current component perpendicular to the original magnetization. This transverse component of the spin current inside a ferromagnet becomes rapidly damped on a typical distance of a few interatomic spacings [73], which is a result of a large exchange splitting that leads to mostly destructive interference effects due to all contributions of wave vectors on the two Fermi surfaces of the ferromagnetic metal. We have concentrated on the most fundamental aspect here: calculation of the torque and its connection to electronic structure of the material where it arises.

We should note that there are several ways to polarize current or generate torque due to currents. Here we cover primarily situations where a second noncollinear magnetic layer is used to polarize the current (Fig. 4.1). Another source of spin polarization represents the spin Hall effect [74, 75]. It originates from the spin-orbit interaction affecting the electron motion and does not require any magnetizing layer. This effect gives rise to the so called the spin-orbit torque [76], initially observed in (Ga,Mn)As [77]. Recently it has been shown to be able to rotate the magnetization in a novel antiferromagnet CuMnAs [61, 78], whose other aspects we have studied in Sec. 3.1. Overall, studies of this effect have recently brought a number of novel discoveries and we refer the reader to specialized literature for more details [79–81].

4.1   Spin-mixing conductance

A successful description of STT related effects has been provided by the magneto-electronic circuit theory [82–84], aimed at treating non-collinear magnetic systems consisting of FM and NM elements (nodes). This scheme is highly efficient especially when dimensions of individual nodes are smaller than the spin-diffusion lengths but bigger than the electron mean-free paths of the corresponding materials. In this model the linear relation between the torque and the spin accumulation is described by the spin-mixing conductance. Significant insight
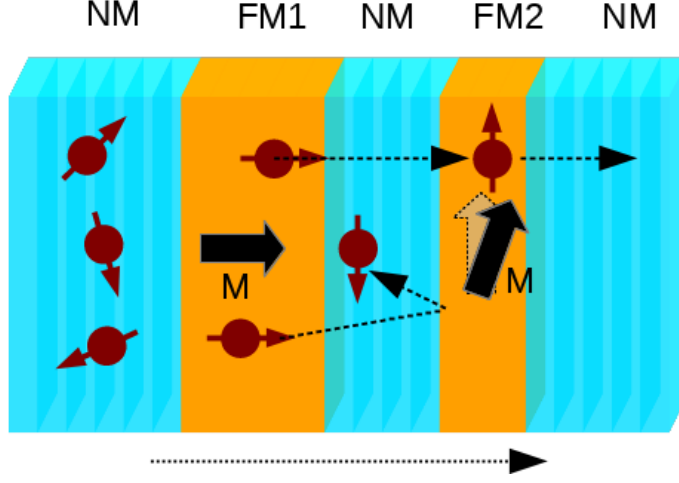
Figure 4.1: Scheme of electron transport in a junction comprising two FM slabs with non-collinear (in this case perpendicular) magnetizations sandwiched by NM leads, and the effect of this transport on magnetization.

can be obtained here by calculating the spin-polarized electronic and transport properties of a single ferromagnet/non-magnet interface [73, 85], which even allows to incorporate interface alloying, but extra assumptions are needed to draw conclusions about the spin mixing conductance.

We have sketched an alternative approach to the mixing conductances that employs the non-equilibrium Green's function (NEGF) formalism [86], applied to a ferromagnetic (FM) layer (with a direction $\mathbf{n}$) embedded between two semi-infinite non-magnetic (NM) leads; one of them contains spin accumulation oriented in the direction $\mathbf{s}$ and represented by a spin-dependent shift of the Fermi level E_s. The torque is given as the time derivative of the total spin momentum: $\boldsymbol{\tau} = -\mathrm{i} \left[\boldsymbol{\sigma}, \hat{H} \right]$. Its derivative w.r.t. spin accumulation in the left lead is provided by the following formula:

$$\frac{\delta \bar{\boldsymbol{\tau}}}{\delta E_s} = 2 \operatorname{Re} C^{\mathrm{mix}} \mathbf{n} \times (\mathbf{s} \times \mathbf{n}) + \tag{4.1}$$
$$2 \operatorname{Im} C^{\mathrm{mix}} \mathbf{s} \times \mathbf{n},$$

where the spin-mixing conductance is given as

$$C^{\mathrm{mix}} = \frac{1}{2\pi} \operatorname{tr} \left[i \left(G_\uparrow^r - G_\downarrow^a \right) \Gamma_{\mathcal{L}} - \Gamma G_\uparrow^r \Gamma_{\mathcal{L}} G_\downarrow^a \right] . \tag{4.2}$$

Here G_s^r, G_s^a are retarded and advanced Green's functions and $\Gamma_{\mathcal{L},\mathcal{R}}$ ... the anti-hermitean parts of the contributions to the self-energy due to the left and right lead, respectively, Γ is their sum [A.7]. Therefore the real and imaginary part of the mixing conductance correspond to the torque component in-plane w.r.t. spin accumulation, and out-of-plane, respectively (Fig. 4.2). The derived general formula is implemented in an *ab initio* technique [A.7].
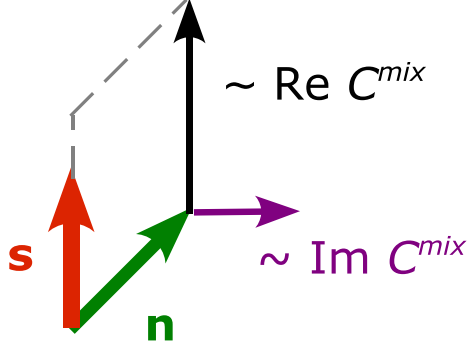
24

Figure 4.2: The relation between the directions of the spin accumulation **s**, magnetization **n**, and the real and imaginary parts of spin-mixing conductance.

The application of this method to standard junctions employed in spintronics: Cu | Ni | Cu, Cu | Co | Cu, Cu | Py | Cu has shown that the real part of spin mixing conductance approaches a saturation value, while the imaginary part approaches zero (Py denotes permalloy with composition $Ni_{0.84}Fe_{0.16}$). This result is in agreement with previous approaches [83, 84], but in the regime before that it provides interesting deviations from that value, and its description goes beyond the more simple approaches as is the Valet-Fert model [88]. Namely we find oscillations, which are most pronounced for the Ni case with (001) orientation[A.7], and well visible in the (111) direction (Fig. 4.3). Its decay length is connected with the variation of the difference between majority and minority spin Fermi surfaces [A.7].

The theory yields particularly interesting results for thin layers composed from Co_2MnSi, a half-metallic material. A significant value of the imaginary part has been found there in combination with Cr as a nonmagnetic layer [87]. This effect originates mainly from specific properties of interface reflection, namely a phase difference acquired between the majority and minority spin reflected electrons [A.8] Another important precondition here is slow variation of this phase difference over a large part of the 2D Brillouin zone (BZ). Fig. 4.4 shows that this condition is fulfilled for the interface with Cr, but not with Vanadium.

Our method allows us to include the effect of chemical disorder in a very efficient way based on the CPA. In this context we have studied for example the effect of interface interdiffusion on the oscillations of C^{mix} shown in Fig. 4.3. Interestingly, these oscillations are rather stable against this type of disorder, but would be destroyed by alloying inside the layer [A.9]. The influence of disorder on epitaxial layers of Co_2MnSi have also been studied, which is especially important when Co_2MnSi is also used to spin-polarize the current [89]. Furthermore, the unusually high imaginary component of C^{mix} in Co_2MnSi survives even strong antisite disorder in this compound, which on the other hand reduces significantly the spin polarization [A.9].

4.2 Complete description of junctions, torkance

The above described theory rests on the need to evaluate spin accumulation near the switched layer. The current is however polarized in another layer which has to be closely located, therefore a spin valve is used (Fig. 4.1). It is also possible to extend the theory in a way that
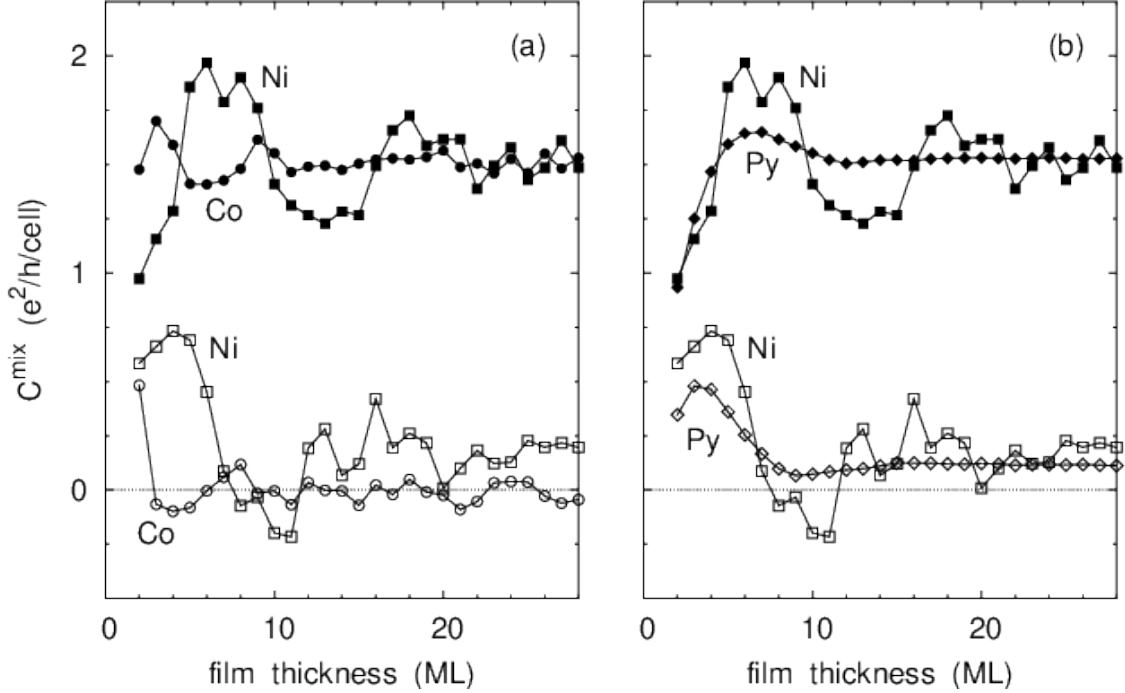
Figure 4.3: Spin-mixing conductances C^{mix} of fcc(111) systems as functions of the magnetic film thickness: (a) Cu/Ni/Cu (squares) and Cu/Co/Cu (circles), and (b) Cu/Ni/Cu (squares) and Cu/Py/Cu (diamonds). The filled and the empty symbols denote respectively the real and the imaginary parts of C^{mix} [87].

the torque is directly calculated from of the whole non-collinear spin valve, in an analogy to the Landauer formula for the ballistic conductance [A.10]. The torque is then related to the applied bias in terms of a linear response coefficient named torkance. The in-plane torkance $C_{\parallel}$ on FM2 is given as

$$C_{\parallel} \sin\theta = \frac{1}{2\pi} \text{Tr} \left\{ \mathbf{n}_1 \cdot \boldsymbol{\sigma} \left(\Gamma_{\mathcal{R}} G^r \Gamma_{\mathcal{L}} G^a - \Gamma_{\mathcal{L}} G^r \Gamma_{\mathcal{R}} G^a \right) \right\}. \tag{4.3}$$

The out-of-plane torkance then requires the calculation of angular derivative of Green's function, G'^r and is given as

$$C_{\perp} = \frac{1}{2\pi} \text{Tr} \left\{ G'^r [\Gamma_{\mathcal{L}} (1 + iG^a \Gamma_{\mathcal{L}}) - \Gamma_{\mathcal{R}} (1 + iG^a \Gamma_{\mathcal{R}})] \right\}, \tag{4.4}$$

hence it contains only reflection-like terms. These quantities can also be expressed in terms of scattering coefficients, in an analogy to the Landauer formula. Then in-plane torkance coefficient (4.3) can be written as

$$C_1 = \frac{1}{2\pi} \sum_{\lambda\rho s s' s''} (\mathbf{n}_1 \cdot \boldsymbol{\sigma})_{s''s'} \left(t_{\rho s',\lambda s} t^*_{\rho s'',\lambda s} - t_{\lambda s',\rho s} t^*_{\lambda s'',\rho s} \right), \tag{4.5}$$

and the out-of-plane torkance (4.4) can be transformed into

$$C_{\perp} = \frac{i}{2\pi} \left(\sum_{\lambda s \lambda' s'} r'_{\lambda' s',\lambda s} r^*_{\lambda' s',\lambda s} - \sum_{\rho s \rho' s'} r'_{\rho' s',\rho s} r^*_{\rho' s',\rho s} \right), \tag{4.6}$$
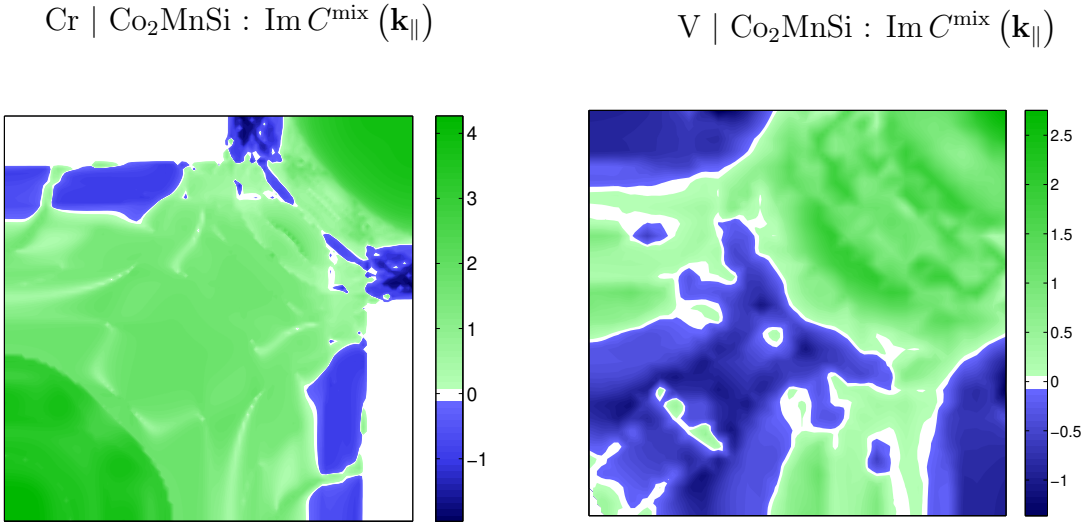
Cr | Co$_2$MnSi : Im $C^{\text{mix}}\left(\mathbf{k}_\parallel\right)$ 　　　　　 V | Co$_2$MnSi : Im $C^{\text{mix}}\left(\mathbf{k}_\parallel\right)$

Figure 4.4: $\mathbf{k}_\parallel$-resolved contributions to the imaginary part of the spin-mixing conductance of systems Cr/Co$_2$MnSi/Cr(100) and V/Co$_2$MnSi/V(100) with a 20 ML thick Co$_2$MnSi film. The square displays one quarter of the full 2D BZ and it is equivalent to two irreducible BZs; the $\bar{\Gamma}$ point is located in the lower left corner, the $\bar{\text{M}}$ point lies in the upper right corner, and the two remaining corners correspond to the $\bar{\text{X}}$ points [A.8].

where $r_{\lambda's',\lambda s}$ $(r_{\rho's',\rho s})$ denote reflection coefficients between states λ (and ρ) of the $\mathcal{L}$ (and $\mathcal{R}$) lead, and $t_{\rho s',\lambda s}$ denotes the transmission coefficient from an incoming state λs into an outgoing state $\rho s'$. The calculation of these quantities has been performed from first principles for several junctions with the switched layer studied in Sec. 4.1. The results show that oscillations of spin-mixing conductance observed for Ni are present in the torkance as well, although they are not seen in the conductance [A.10].

In the studied junctions with two ferromagnetic layers, one can replace the separating non-magnetic metal by a thin insulating barrier. This can help to increase the current spin polarization if its properties would allow a filtering effect suppressing specific spin channel, as observed for tunneling in the nowadays standard Fe/MgO junctions. We have studied a newly proposed Fe/LiF junction, whose advantage is a good matching between the Fe and LiF lattices, and we show its ability to reach a very high spin polarization [A.11].

28

Chapter 5

Ultrafast magnetization dynamics

For a comprehensive picture of the field of ultrafast magnetization dynamics I recommend overviews [9, A.12], here I concentrate mainly on aspects related to computational condensed matter theory. A highly debated point has been the connection between magnetization dynamics and heating of phononic system, therefore I open this chapter by presenting our several contributions related to this point. Notably, most works in this field have studied canonical $3d$ electron based transitional metal ferromagnets. Systems with $4f$ electrons exhibit significant differences, novel theoretical concepts have to be considered, and they are thus studied in a separate Section 5.2. Magnetization dynamics is necessarily connected with spin currents, and we show in the next Section that there are several different mechanisms involved. A part of it also considers noncollinearity and thus connects the field of ultrafast generated spin currents with the problem of spin torques presented in Chapter 4. While all mechanisms discussed so far have essentially thermal character, there are also non-thermal effects typically dependent on light helicity, and these together with other aspects connected to optics are discussed in the last two Sections.

5.1 The role of phonons

Naively, phonons may not seem to play role when considering ultrafast demagnetization since they are usually not connected with any angular momentum. However, they have the highest thermal capacity from all subsystems in a typical condensed matter, which alone renders them to be important here. Furthermore, an excess angular momentum is assumed to be ultimately transferred to the lattice, here one can expect that an analogue of the Einstein-de Haas experiment [8] would take place on the ultrafast timescale [90]. An important point to take into account is the angular momentum of phonons, whose role in spin relaxation has been studied recently [91].

One of the mechanisms of ultrafast demagnetization that has gained a widespread support employs Elliott-Yafet (EY) spin flips [92] on phonons [93–95]. Spin-orbit interaction is the precursor here. In order to study spin non-conserving processes in a ferromagnetic crystalline solid, we note that its eigenstates $\left|\Psi_{\mathbf{k}n}^{\uparrow}\right\rangle$, $\left|\Psi_{\mathbf{k}n}^{\downarrow}\right\rangle$ can be decomposed into pure spin states consisting of its spin- majority and minority parts:

$$\left|\Psi_{\mathbf{k}n}^{\uparrow}\right\rangle = a_{\mathbf{k}n}^{\uparrow}\left(\boldsymbol{r}\right)\left|\Uparrow\right\rangle + b_{\mathbf{k}n}^{\uparrow}\left(\boldsymbol{r}\right)\left|\Downarrow\right\rangle, \; \left|\Psi_{\mathbf{k}n}^{\downarrow}\right\rangle = a_{\mathbf{k}n}^{\downarrow}\left(\boldsymbol{r}\right)\left|\Downarrow\right\rangle + b_{\mathbf{k}n}^{\downarrow}\left(\boldsymbol{r}\right)\left|\Uparrow\right\rangle, \tag{5.1}$$

where $\left|\Uparrow\right\rangle$ and $\left|\Downarrow\right\rangle$ are eigenstates of the operator of spin projection along the $z$axis, and
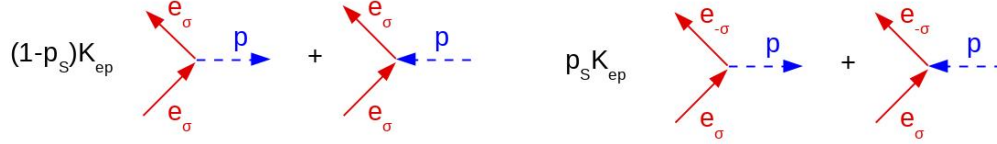
Figure 5.1: Electron-phonon scattering: emission and absorption. Spin flip occurs with probability p_S

$a_{\mathbf{k}n}^{\sigma}(\boldsymbol{r})$ and $b_{\mathbf{k}n}^{\sigma}(\boldsymbol{r})$ $(\sigma =\uparrow,\downarrow)$ are projections of $\left|\Psi_{\mathbf{k}n}^{\sigma}\right\rangle$ to spin subspaces σ and the other one, respectively. Minority components $b_{\mathbf{k}n}^{\sigma}(\boldsymbol{r})$ are generally nonzero if spin-orbit coupling is present, and represent the degree of spin-mixing. This spin-mixing then makes transitions into a state with different dominant spin possible (Fig. 5.1). A relation between spin lifetime τ_S for a general kind of scattering event with lifetime τ can be derived [92, 96], employing several assumptions: paramagnetic metal, small variations of electron-phonon matrix elements and $b_{\mathbf{k}n}$ in BZ, $b_{\mathbf{k}n}^{\sigma} \ll a_{\mathbf{k}n}^{\sigma}$ [96]. This relation called after Elliott employs the Fermi-surface (FS) averaged spin-mixing of eigenstates $\langle b^2 \rangle = \sum_{\sigma,n} \int |b_{\mathbf{k}n}^{\sigma}|^2 \tilde{\delta}(E_{\mathbf{k}n}^{\sigma} - E_F)$ and predicts the spin-flip (SF) probability $p_S^{b^2}$ to be:

$$p_S^{b^2} = \frac{\tau}{\tau_S} = 4\left\langle b^2 \right\rangle \tag{5.2}$$

This model was found to predict correctly the observed relation between the demagnetization rates in Ni, Co and Gd [95], however a number of parameters in the whole picture of demagnetization had been fitted. We have developed a method for a more accurate calculation of this process, a first principles calculation of electron-phonon scattering taking into account the electron population modified due to a laser. This method employs the SF Eliashberg function [97]. The scheme has been extended to handle excited states, which is crucial to understand processes in systems excited by a laser.

The evolution of spin populations is driven by an initial electron repopulation induced by the pump laser. We describe this redistribution by band-independent occupation factors $f_\sigma(E)$, thus catching the key quantities of pumped electron system - its spin and energy dependence. Assumption that all states given by σ and E have the same occupancy is partially justified by the simple band structure of the studied metals in the region above E_F [98]. It is possible to go beyond this approximation with the presented method, but at the cost of significant numerical complications.

The Eliashberg function is usually defined for equilibrium, thus assuming only electrons at the Fermi level. We generalize this concept and define the spin- and energy-dependent generalized spin-flip Eliashberg function, expressed from spin-resolved electron-phonon matrix elements $g_{\mathbf{k}n,\mathbf{k}'n'}^{\nu\sigma,\sigma'}(\mathbf{q})$ employing reasonable approximations [A.13]. This leads to its formulation analogous to the one in equilibrium case [97]:

$$\alpha_{\uparrow,\downarrow}^2 F'(E,\Omega) = \frac{1}{2M|\Omega|} \sum_{\nu,n,n'} \int d\mathbf{k} \int d\mathbf{k}' g_{\mathbf{k}n,\mathbf{k}'n'}^{\nu\uparrow,\downarrow}(\mathbf{q})\,\delta(\omega_{\mathbf{q},\nu} - |\Omega|)\,\tilde{\delta}\left(E_{\mathbf{k}n}^{\uparrow} - E\right)\tilde{\delta}\left(E_{\mathbf{k}'n'}^{\downarrow} - E\right)$$
$$\tag{5.3}$$

where $\tilde{\delta}$ is a broadened delta function. The broadening allows us disregard the change of energy due to phonon emission/absorption and therefore it has to be higher than 50 meV (a higher value is anyway typically used for good convergence of numerical codes). We define

$w_{\sigma\sigma'}(E)$, a spin- and energy-dependent scattering rate defined as the average over all available states at a given energy E and all phonon states (or equivalently over destination states):

$$w_{\sigma\sigma'}(E) = \int_0^\infty d\Omega \alpha^2_{\downarrow\sigma,\sigma'} F'(E, \Omega) (1 + 2N(\omega_{\mathbf{q},\nu})) , \qquad (5.4)$$

where $N(\omega_{\mathbf{q},\nu})$ describes the occupation factor of phonons with energy $\omega_{\mathbf{q},\nu}$. Then $w_{\uparrow\downarrow}(E) = w_{\downarrow\uparrow}(E) = w_S(E)$ since the same is valid for $\alpha^2_{\uparrow,\downarrow} F'(E, \Omega)$ [A.13]. The spin-resolved transition rates are $S_{\sigma\sigma'} = \int w_{\sigma\sigma'}(E) f_\sigma(E) (1 - f_{\sigma'}(E)) dE$. Therefore the spin decreasing rate $S^{\uparrow\downarrow}$ and spin decreasing rate $S^{\downarrow\uparrow}$ are given by formulas that differ only by occupation factors:

$$S^{\uparrow\downarrow} = \int w_S(E) f_\uparrow(E) (1 - f_\downarrow(E)) dE$$

$$S^{\downarrow\uparrow} = \int w_S(E) f_\downarrow(E) (1 - f_\uparrow(E)) dE$$

Then $w(E) = \sum_{\sigma\sigma'} w_{\sigma\sigma'}(E)$ provides the total ep scattering rate. This allows us to define the spin-flip probability for electron at a given energy E during EY scattering (Fig. 5.1) as: $p_S(E) = w_S(E)/w(E)$. The total SF probability is then

$$P_S = (S^{\uparrow\downarrow} + S^{\downarrow\uparrow}) / \sum_{\sigma\sigma'} S^{\sigma\sigma'} \qquad (5.5)$$

The demagnetization rate given as $\mathrm{d}M/\mathrm{d}t = 2\mu_B (S^{\uparrow\downarrow} + S^{\downarrow\uparrow})$ is the most important quantity for demagnetization. Here we have considered only changes of local spin momentum (longitudinal excitations), therefore microscopic momentum change ΔS and macroscopic momentum change ΔM is approximately equivalent. We can also ask about the difference between spin decreasing and increasing processes and introduce a relative quantity called demagnetization ratio, independent of the total electron-phonon rate:

$$D_S = (S^{\uparrow\downarrow} + S^{\downarrow\uparrow}) / \sum_{\sigma\sigma'} S^{\sigma\sigma'} \qquad (5.6)$$

This calculation has been implemented in ELK, an ab initio computational program developed in Halle and Uppsala. Its ability to reproduce previous results [97] for a simple metal - aluminium - has been verified. The implementation of the SF Eliashberg function based on ab initio electron-phonon coupling matrix elements represents a significant improvement of the demagnetization rate calculation accuracy. The limitations of this calculation first of all result from the numerical requirements, since a large supercell is needed, but the complexity of calculations scales cubically with the size of the supercell. This calculation method has provided material-specific quantitative information about spin-flip processes during electron-phonon scattering, for the first time also for a system in non-equilibrium state due to the pump laser. We have found that the spin-flip probability depends strongly on electron energy with much higher value for deeper lying holes than for electrons near the Fermi level or above it, as shown in Fig. 5.2. Furthermore, for a wide range of electron energies the Elliott relation overestimates the real spin-flip probability in Ni. Overall the agreement with the simplified Elliott relation for SF probability (Eq. 5.2) is limited, as shown in Fig. 5.2, and it has to be applied with caution. Generally, the spin-flip probability drops below 2.5% for states above
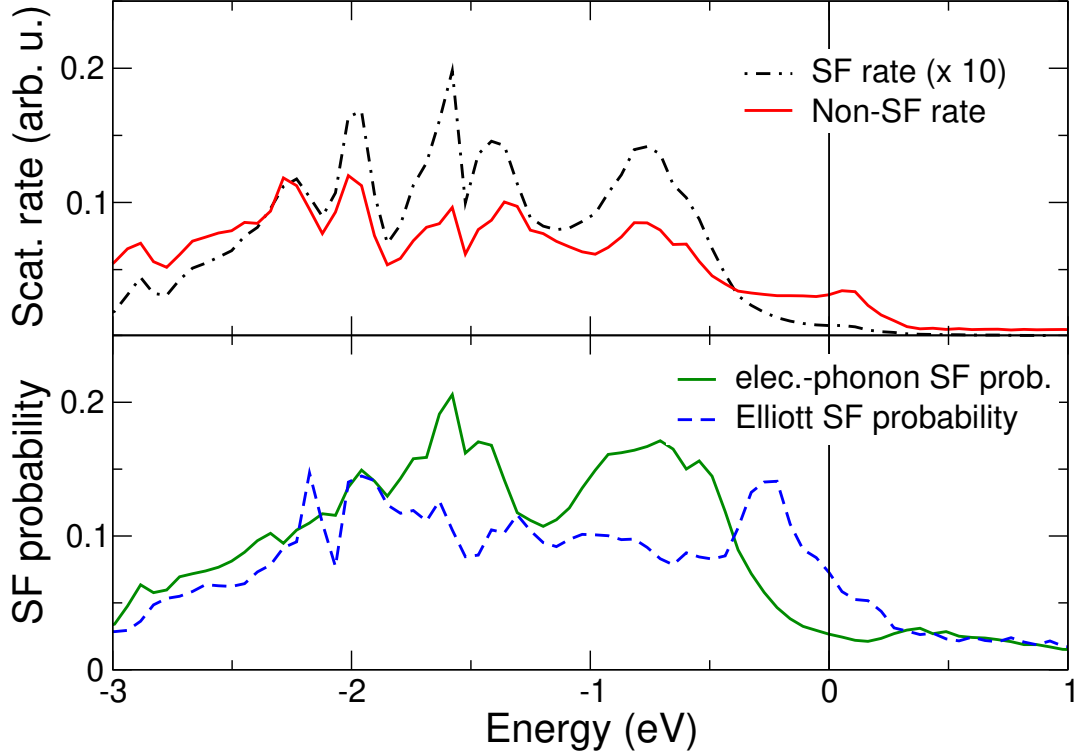
Figure 5.2: Energy-resolved electron-phonon total and SF scattering rates $w(E)$ and $w_{\uparrow\downarrow}(E)$ of Ni (top), and normalized SF probability $P_S(E)$ and approximate SF probability $P_S^{b^2}(E)$ obtained from the Elliott relation (bottom). Reprinted figure from [A.14].

the Fermi level, but it can reach values higher than 10% for states lying more than 0.25eV below the Fermi level [A.14]. These findings help to understand the possible contribution of Elliott-Yafet processes to the ultrafast demagnetization.

This energy dependence and the estimated laser-induced redistribution of electrons has been used to calculate the demagnetization rate for Ni. This led to a conclusion that the Elliott-Yafet mechanism is much more efficient for non-thermal electron distributions present just after the pump pulse than for any thermalized one, for which the demagnetization rate drops below 0.1 μ_B per ps and atom (slower than equilibration with lattice) in the case of Ni (Tab. 5.1). Therefore the Elliott-Yafet mechanism of demagnetization is completely non-thermal on femtosecond timescale. The two (or three) temperature model that we discuss in the following Subsection is thus inapplicable to it. The main reason for that is the much higher SF probability in deep lying states, significantly available only in non-thermal state. Furthermore, spin increasing and decreasing transitions largely cancel out in the energy region below the Fermi level for the thermalized state, as indicated by low value of D_S in Tab. 5.1. Fig. 5.3 demonstrates these findings schematically

Material-specific quantitative information about spin-flip processes during electron-phonon scattering for two more important ferromagnetic metals Fe and Co has subsequently been evaluated, which led to a calculation of their demagnetization rate [A.13]. Summary of results for Fe, Co and Ni is reprinted in Tab. 5.1. The calculations were done using the above implementation of the SF Eliashberg function based on ab initio electron-phonon coupling matrix elements and considering the excited states occupied due to laser pumping. The main finding for Ni, that the Elliott-Yafet mechanism is much more efficient for non-thermal elec-

Table 5.1: Given are *ab initio* calculated spin-flip probabilities P_S, Elliott SF probability $P_S^{b^2}$, demagnetization ratios D_S, and relative demagnetization fractions $\Delta M/M_0$ for laser-pumped Ni, Fe, and Co. Calculated values are given for equilibrium (low T), for thermalized electrons at a high Fermi temperature T_e, and for the nonequilibrium (NEQ) electron distribution created by fs laser-excitation. Computed values for the approximate Elliott SF probability $P_S^{b^2}$ are compared to values by [99] (in brackets, marked with *). The demagnetization fraction $\Delta M/M_0$ relative to the equilibrium magnetization M_0, achieved by electron-phonon SF scattering, is given in % at 250 fs [A.13].

	$P_S^{b^2}$	P_S	D_S	$\Delta M/M_0$
Ni (low T)	0.07 (0.10 *)	0.04	0	0
Ni (T_e=3000 K)	0.11	0.07	0.003	3.1
Ni (NEQ)	0.12	0.09	0.025	16.7
Fe (low T)	0.068 (0.096 *)	0.04	0	0
Fe (T_e=3000 K)	0.13	0.09	0.008	4.5
Fe (NEQ)	0.14	0.07	0.030	11.4
Co (low T)	0.060 (0.044 *)	0.010	0	0
Co (T_e=3000 K)	0.095	0.017	0.002	0.9
Co (NEQ)	0.105	0.022	0.010	2.3

tron distributions present just after the pump pulse than for any thermalized one remains valid for these cases too. As a part of this work electron-phonon lifetimes and spin lifetimes for all the 3 mentioned metals had been calculated. More attention was also given to the testing of the so called Elliott relation (approximation) [A.13]. The calculated demagnetization rates are weaker than those extracted from experiments and this finding suggests that Elliott-Yafet like spin-flips on phonons do not represent the main mechanism responsible for the observed ultrafast demagnetization. However, we should note that all these calculations were performed in the limit of small perturbations of the ground state due to laser. Beyond this approximation more complex behavior may occur [100, 101].

5.1.1 The three temperature model and beyond

It is clear that the phononic system is strongly related to demagnetization and it is thus desirable to gain a deeper insight into it. In common ultrafast magnetization dynamics models it has been described by the lattice temperature (T_l), which together with the electronic temperature (T_e) forms the established two temperature model (2TM) [102]. This has to be extended by adding spin system temperature T_s associated to magnetization, leading to the three temperature model (3TM), an approach sufficient to gain a thermodynamical insight into fs demagnetization [7]. The spin system temperature T_s is defined as the temperature corresponding to the achieved magnetization according to the standard equilibrium $M(T)$ dependence. The coupling of the different subsystems is shown in the following equations, providing the temporal evolution of the temperatures:
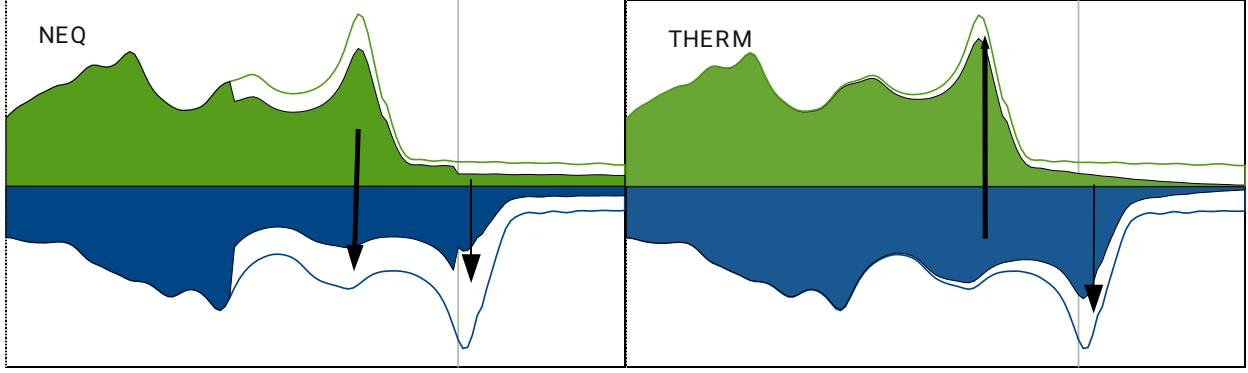
Figure 5.3: Spin-resolved DOS (filled areas) and phonon induced spin-flips (arrows) of NEQ and electron thermalized Ni. The equilibrium DOS is shown by thin lines. SF transitions are significantly different at energies above and below E_F. The arrows thickness corresponds to the transition rate, its direction and length give which direction is dominant and how much. The amount of laser redistributed electrons has been enlarged to improve visibility. Reprinted figure from [A.14].

$$
\begin{aligned}
C_e \frac{\partial T_e}{\partial t} &= G_{el}(T_l - T_e) + G_{es}(T_s - T_e) + P(t) \qquad (5.7) \\
C_l \frac{\partial T_l}{\partial t} &= G_{el}(T_e - T_l) + G_{ls}(T_s - T_l) \\
C_s \frac{\partial T_s}{\partial t} &= G_{se}(T_e - T_s) + G_{ls}(T_l - T_s),
\end{aligned}
$$

where C_e, C_l, C_s are electronic, lattice, and spin system heat capacities, respectively. G_{el}, G_{es}, G_{ls} are the electron-lattice, electron-spin and spin-lattice coupling constants, and $P(t)$ is the laser source term [7].

The underlying assumption for this approach is that these systems are internally thermalized. For the lattice much information about the thermalization were not available until recently, and there was a strong need to examine the thermalization timescale. The observation of phonon propagation following their ultrafast generation by the group of H.A. Durr from Stanford Institute for Materials and Energy Sciences, SLAC represents an important step here. They have detected coherent acoustic phonons generated during ultrafast laser excitation of ferromagnetic bcc Fe films grown on MgO(001). This has allowed to observe population of individual phononic modes on the ps timescale. A calculation of excitation rates and lifetimes for different phononic modes allows us to predict the distribution of these modes. In agreement with the experiment we conclude that the population of phonons remains nonthermal for significantly long times (>1 ps), and the use of temperature based description on this timescale may cause big errors [103].

Several works published in the last few years examine the deviation of the phonon population from the thermalized one in more detail [A.15, 104, 105]. We have calculated the dependence of the electron-phonon interaction on phonon mode and $\boldsymbol{k}$ vector. It is rather strong, as shown in Fig. 5.4 for FePt. On the other hand, phonon-phonon interaction is overall generally weaker and does not lead to thermalization within the studied timescales of 10 ps order. From these we obtain phonon populations that differ sharply from the thermal
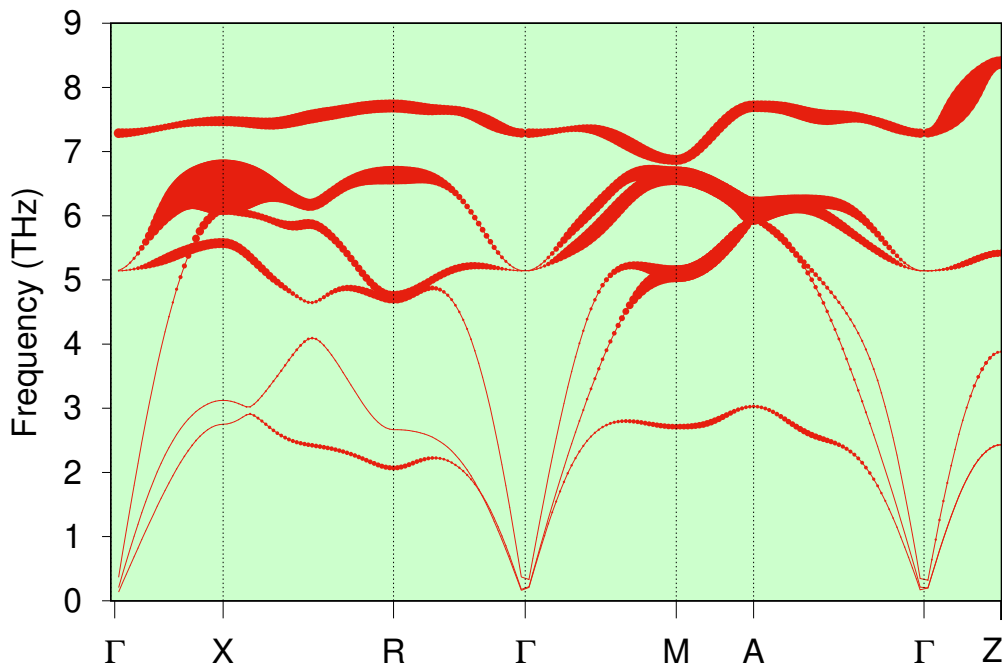
Figure 5.4: Calculated phonon dispersions of ferromagnetic FePt along high-symmetry lines in the simple tetragonal BZ. The symbol size is proportional to the magnitude of the mode-dependent electron-phonon coupling function G_Q at 300 K [A.15].

ones within picoseconds after the pump [A.15]. Fig. 5.5 shows that the lattice remains out of equilibrium for long time scales ($\sim$ 100 ps). This allows to improve understanding of recent experimental observations and disproves the applicability of the model based on one lattice temperature here [103].

An interesting playground to observe the effect of ultrafast laser irradiation on lattice are magnetic nanoparticles. A significant anisotropy of size change was observed in FePt nanoparticles upon the action of laser pump, in fact the lattice shrinks along the c-axis, while it expands along a, b axis. After about 3ps the lattice parameter c starts to revert back to its original value, while a remains expanded for longer times. This unexpected behavior reveals that on such short timescales the relation between lattice dimensions and magnetization cannot be described just by the standard magnetostriction theory [A.16]. Ab initio calculations of the induced stress including the non-equilibrium phonon population recover this behavior when coupled together with a magnetic stress. Magnetic stress corresponds to the tendency to modify lattice parameters to those of a paramagnetic state, described here by the DLM method (Sec. 2.2). Our analysis allows us to suggest that the effect of magnetoelastic stress is seen on a sub-ps timescale, while later within ps the increasing occupation of phononic modes leads the system to a different type of deformation. These findings can be used to design new types of THz frequency magnetostrictive actuators.

5.2 Demagnetization in systems with $4f$ orbitals

There are several fundamental differences from the magnetization dynamics point of view between the moments of $4f$ and $3d$ electrons: $4f$ states are located deep under the Fermi
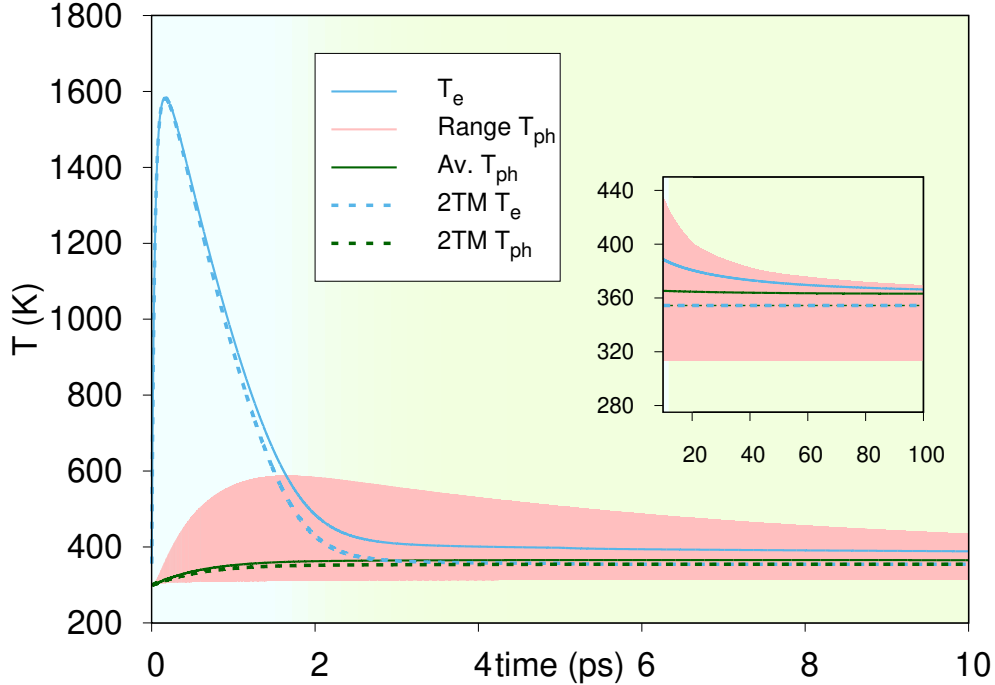
Figure 5.5: *Ab initio* calculated temporal evolution of the electronic temperature (blue line), average phonon temperature (green line) and temperature range within which all the phonon-mode temperatures are contained (red area). The inset shows the temporal evolution from 20 to 100 ps. Dashed lines show the results of the 2TM solved with *ab initio* calculated input parameters for FePt [A.15].

level, they are very rigid and thus serve as a perfect example of a Heisenberg ferromagnet. $4f$ moments interact usually indirectly via the more itinerant $3d$ electron shell (although it has a much smaller moment). $4f$ states can also possess a significant orbital angular momentum - this point can be crucial for explaining the different dynamics between Gd and Tb, which also differ significantly in terms of orbital momentum - the former one possess $L = 0$, while the latter $L = 3$.

Some of the works attempting to describe magnetization dynamics in these systems ignore the above mentioned important aspects, basically not distinguishing between metals containing $4f$ and $3d$ orbitals [95]. In our work we separately keep track of momenta associated to $4f$ states and the remaining valence states, partially inspired by the success of the so called opencore model, where $4f$ states are separated in a similar way when calculating the electronic structure. Although the coupling between these moments is very strong since valence momentum is basically induced by that of $4f$ states, one can ask whether these moments would not align differently in the strong non-equilibrium situation following the laser excitation. This could be considered to be a specific excitation of this coupling, and thus allowing also a deeper insight into rare-earth metals.

Such problem can be mapped to an effective Heisenberg Hamiltonian (Eq. 2.1) generalized to separate contributions from different orbitals (Fig. 5.6):

$$\mathcal{H} = -\sum_{\langle ij \rangle} \frac{J_{ij}}{2} \mathbf{S}_i \cdot \mathbf{S}_j - \sum_{i \in \mathrm{Gd}} J_{int} \mathbf{S}_i \cdot \mathbf{S}'_i - d_z \sum_i (S_i^z)^2. \tag{5.8}$$
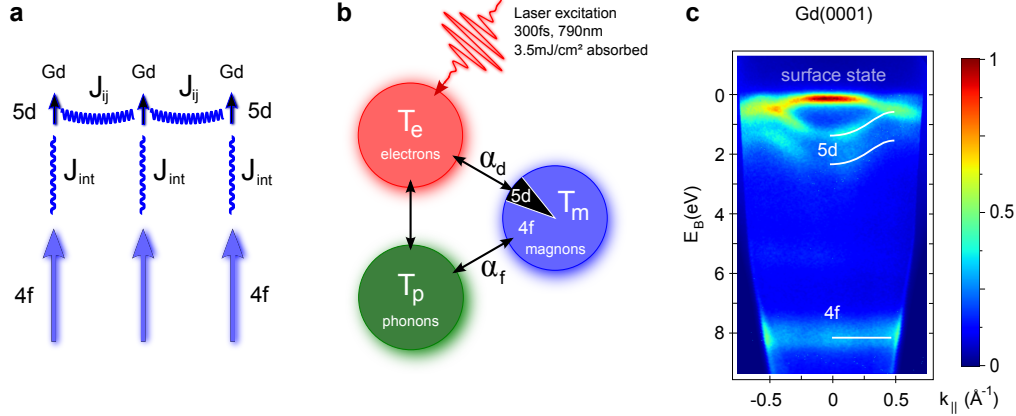
36

Figure 5.6: **Couplings of the gadolinium spin system. a)** 5d and 4f spin systems couple via inter- and intra-atomic exchange, where the intra-atomic exchange $J_{\text{int}} = 130$ meV is much larger than the largest (nearest-neighbor) inter-atomic exchange $J_{ij} = 5.9$ meV. In thermal equilibrium the combination of inter- and intra-atomic exchange interactions mediates spin order in the 4f system via the delocalized 5d valence bands. Upon femtosecond laser excitation the dynamics of the 5d spin system is dominated by the coupling α_{e} to the hot valence electrons, while the localized 4f spins couple only to the phonon bath via α_{p}. **b)** The binding energy *vs.* parallel momentum map $E_{\text{B}}(k_{\parallel})$ of Gd recorded with higher order harmonic radiation ($\hbar\omega = 36.8$ eV) in time- and angle-resolved photoemission gives simultaneously access to the transient exchange splitting of the 5d minority and majority spin bands ($\downarrow$ and $\uparrow$) and the magnetic linear dichroism of the localized 4f state [A.17].

We have calculated the relevant exchange interactions between atomic moments as well as the intraatomic exchange between Gd $4f$ and $5d$ orbitals using ab initio methods [A.17]. The presence of strong correlation in $4f$ electrons presents a challenge for theory, such systems have been calculated either with the inclusion of Hubbard U [106], or the Hubbard-I approximation [107]. An alternative is to put $4f$ electrons into the core within the opencore treatment, then Gd properties can be successfully reproduced employing the LSDA method [108, 109]. We have used this approach for the interatomic interaction calculation as well.

An important point here is the character of Gd $5d$ moments. Originally it was believed that this moment scales with the effective field and magnetization in Gd, and thus it vanishes at T_C (Stoner-like behavior) [110, 111]. This was however opposed by theoretical calculations [112], as well as later spin- and angle-resolved photoemission experiments [113] finding a finite exchange splitting of the itinerant band in Gd at T_C. A subsequent calculation based on the DLM method (Sec. 2.2) confirms the presence of this splitting at T_C, and argues that the interaction of $5d$ states with the local on-site $4f$ moment and with the surrounding environment is comparably strong [108]. On the other hand, it is clear that the $5d$ moment is not rigid, and therefore it cannot be described with the original Heisenberg model. Therefore we calculate the $5d$ exchange splitting for different angles ϑ w.r.t. $4f$ momentum and include the corresponding momentum change in the modified Heisenberg model. The momentum is found to follow approximately the $\cos\vartheta$ function for $\vartheta < 0.6$ rad, and atomistic simulations indicate that $5d$ moments do not deviate from $4f$ moments further that that in the studied case. Otherwise a total collapse of this moment can be expected [114].

A simulation of the system described by the Hamiltonian (5.8) based on the Landau-

Lifshitz-Gilbert equation (done in collaboration with University of Konstanz) has shown distinct magnetization dynamics of $4f$ and $5d$ orbitals [A.17]. Their dynamics differ by one order of magnitude, with decay constants of 14 vs. 0.8 ps., in a reasonable agreement with experiment. There, most of the $5d$ magnetization dynamics takes place within a rapid 1ps jump , the $4f$ magnetization decrease is represented by a rather linear evolution spread over tens of ps (Fig. 5.7). This represents the first observation of disparate magnetic behavior of intraatomic parts of magnetic moment [A.17]. Notably, the success of this model in explaining the ultrafast response of Gd furthermore confirms the non-Stoner behavior of Gd itinerant band. This distortion of the equilibrium order between the two subsystems significantly contributes to understanding the different observed timescales related to magnetization dynamics in Gd. Note that the orbital-resolved model has also been used to study Gilbert damping in Gd [115].
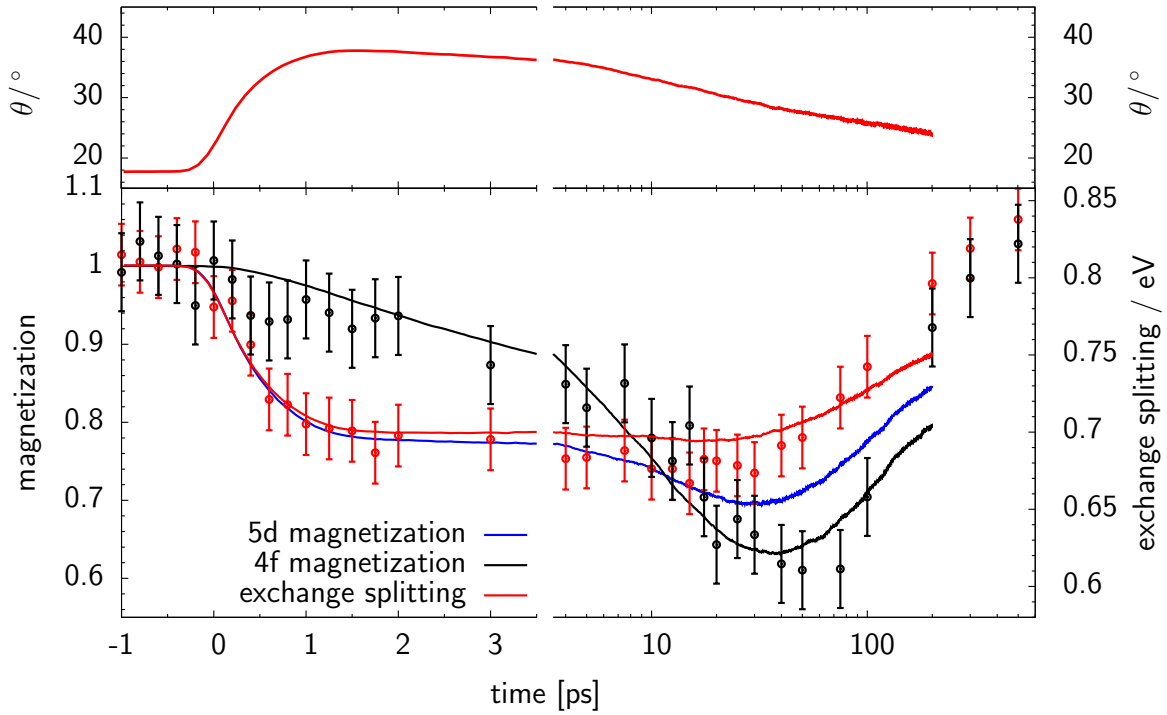

Figure 5.7: Spin dynamics in gadolinium. Normalized exchange splitting of the 5d states (black circles) and magnetic linear dichroism of the 4f state (green dots) are shown as a function of pump-probe delay recorded with 100 fs XUV pulses. The pump pulse has a photon energy of 1.55 eV and was stretched to 300 fs pulse duration. The absorbed fluence is $3.2\,\mathrm{mJ/cm^2}$. Solid lines are calculated with our orbital-resolved spin model. The decoupling of the intra-atomic exchange is demonstrated by the significantly different demagnetization times of the 5d and 4f spin system. Single exponential fits give time constants of 0.8 and 14 ps, respectively. Note that after 3.5 ps the dynamics is displayed on a logarithmic scale to cover the cooling back to the initial sample temperature of 90 K [A.17].

One of the major breakthroughs in the field of ultrafast magnetization dynamics has been discovered in an alloy of a $4f$ system, GdFeCo ferrimagnet. Instead of just a magnetization reduction, a complete magnetization reversal has been achieved in this material [116] with a linearly-polarized laser pulse, without the help of external field, circular polarization of the laser pulse or any other direct source of angular momentum [117]. Interestingly, application
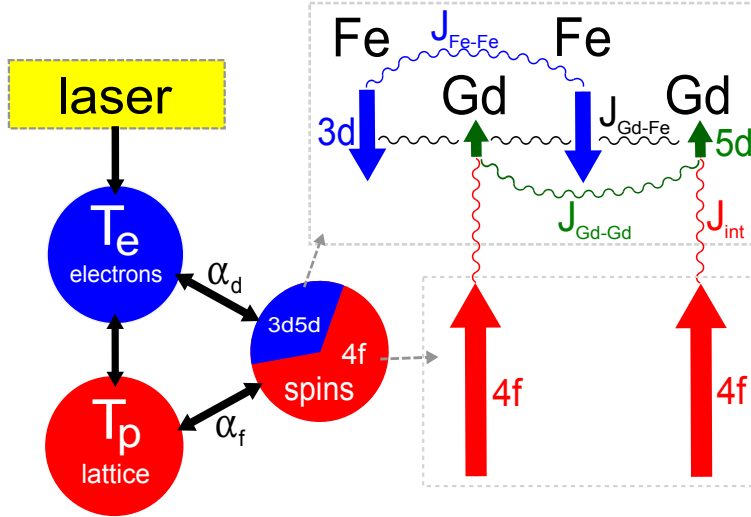
Figure 5.8: Sketches of the orbital-resolved spin model, distinguishing spins stemming from electrons in $5d$ and $4f$ orbitals of Gd (right-hand panel), and the coupling of the spin system to the electronic and phononic heat baths (left-hand panel). Reprinted figure from [A.18].

of another such pulse reverts the magnetization back, so the process can be called toggle switching. It has been demonstrated in many similar materials later. Since this topic cannot be described within the limited scope of this work, we again refer the reader to review literature [9, A.12] and describe here only the theoretical model that we applied to this problem.

We have calculated exchange interaction between the components of the compound and furthermore also the intraatomic exchange between Gd $4f$ and $5d$ orbitals mentioned above (Fig. 5.8 shows the scheme of all considered interactions). A subsequent magnetization dynamics simulation based on the LLG equation (Eq. 2.3) has reproduced the switching behavior, see Fig. 5.9. The simulation also shows the presence of the transient ferromagnetic state [10]. We have demonstrated that the exchange coupling between $4f$ and $5d$ states in Gd is sufficient to revert the large magnetic moment of Gd $4f$ shell on a picosecond time scale. Our simulation is in agreement with a recent finding that the crucial part of magnetization dynamics is dissipationless, driven by exchange interaction [A.18]. According to this simulation the transient ferromagnetic state is reached only if the value of Gilbert damping α_G is sufficiently low so that exchange interaction dominates over damping. Dissipationless magnetization dynamics allows one of the sublattices to be reversed at the expense of the same amount of momentum from the other one.

5.3   Ultrafast spin currents

We have studied theoretically electron motion during demagnetization by means of a semi-classical approach employing different lifetimes and velocities of excited electrons calculated by ab initio methods [118]. This has led to a discovery of a mechanism of a new source of
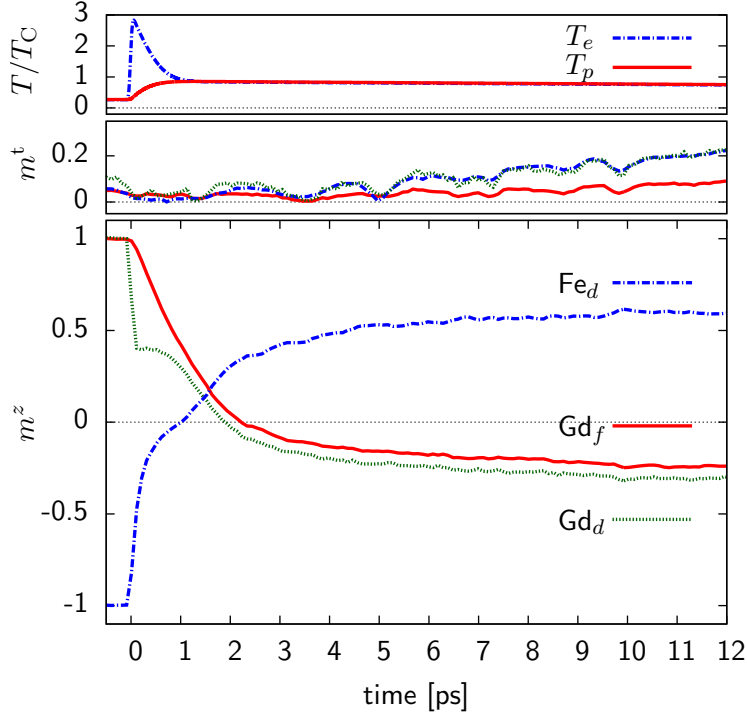
Figure 5.9: Thermally driven switching of the sub- lattice magnetization in GdFe, using a spin model of 81 000 atoms distinguishing magnetization stemming from $5d$ and $4f$ orbitals of Gd and $3d$ orbitals of Fe. Electron (T_e) and phonon (T_p) temperatures are shown as well as the transverse (m^t) and longitudinal (m^z) magnetization dynamics of the different sublattices and orbitals. Reprinted figure from [A.18].

spin current [A.19]. The presence of this laser induced spin current (LISC) can in fact explain the observed decrease of magnetization on fs timescale in some cases.

Generation of LISC requires no external electric field apart from the one present in the pump laser, and it rests on the strong spin dependence of lifetimes and velocities of excited electrons [A.19]. A complete description of the process has to include the motion and energy decay of individual excited electrons on a larger spatial scale where a semi-classical model is applicable, while individual scattering events and their probabilities are described quantum mechanically. The ultrafast diffusion of spin-polarized particles is described without using the limits of infinitely short lifetimes and mean-free paths and infinitely large velocities (as assumed in the standard thermal diffusion equation). On the other hand the electron motion cannot be treated as ballistic due to the high number of scattering events and the model therefore operates between the ballistic and diffusive limit. The predicted magnetization evolution in Ni agrees well with the experimentally measured one, see Fig. 5.10.

More detailed analyses of the effect for different ferromagnetic materials and different substrates have been performed, providing a temporal and spatial distribution of spin momentum in a pumped heterostructure [A.20], as shown in Fig. 5.11. The model has later been extended to include interfacial reflections within the hot electron transport [120].

Generation of spin currents also means that the action of laser can also change magnetization away from the laser spot, and even allows to invoke torques on a separated magnetic
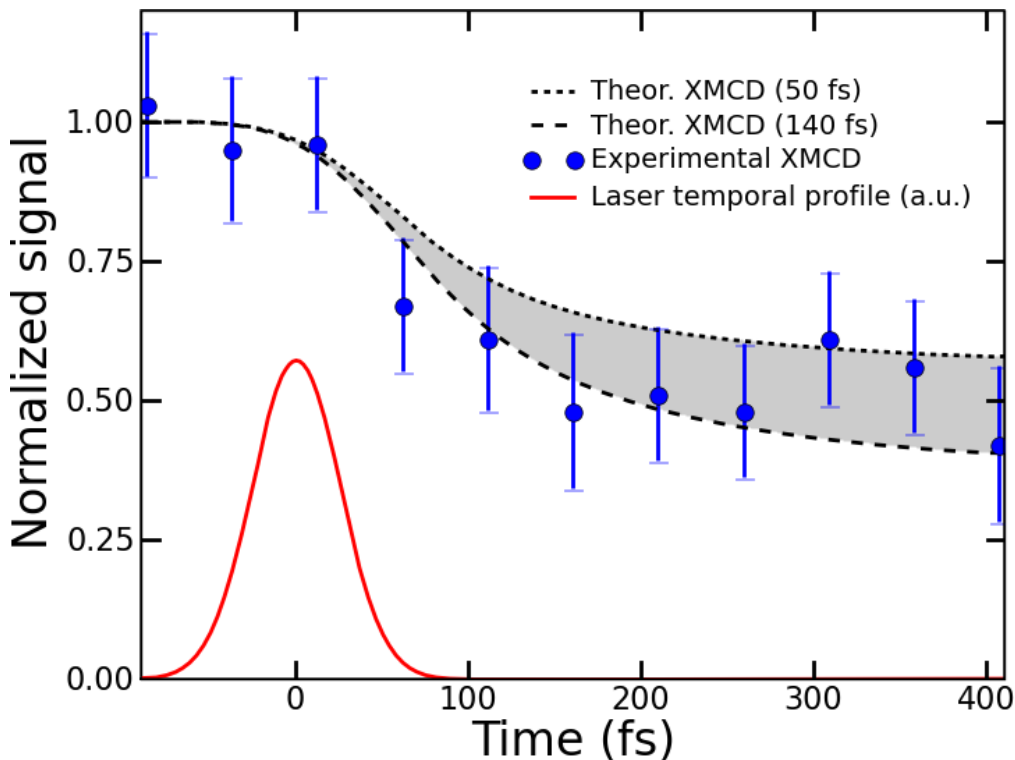
Figure 5.10: Computed laser-induced demagnetization in Ni [A.19]. The shaded area shows where the theoretical result is expected to be (depending on the inelastic lifetime). For comparison we also show recent experimental XMCD data [119]. The used time structure of the laser pulse (in a.u.) is depicted by the red solid line.

layer as discussed further. Compared to its electrical field induced counterpart (FISC), LISC has a number of different features. First of all it allows magnetization dynamics also for a collinear magnetic setup, it can not only rotate magnetization (transversal change) but also change its magnitude (longitudinal change), and depending on the alignment of magnetic layers it can even increase the magnetization to values not observed before for the given metal [11], as shown in Fig. 5.12. The combined experimental and calculated data related to this effect [11] represent one of verifications of our model, other verifications have followed [121–123].

An interesting prediction of our model is the temporal shape of LISC pulses, that is otherwise hard to obtain and could have a big potential in spin electronics since it fits in the THz range. It can be also modified by materials subsequently traversed by this current, and the type of scattering influences the pulse oscillation period and decay rate. The temporal profile of such current has been measured, finding a significant dependence on the cap layer. The addition of ruthenium cap layer leads to a considerably longer spin current pulse than for the the gold cap since ruthenium d states have a much lower mobility than gold sp states [124].
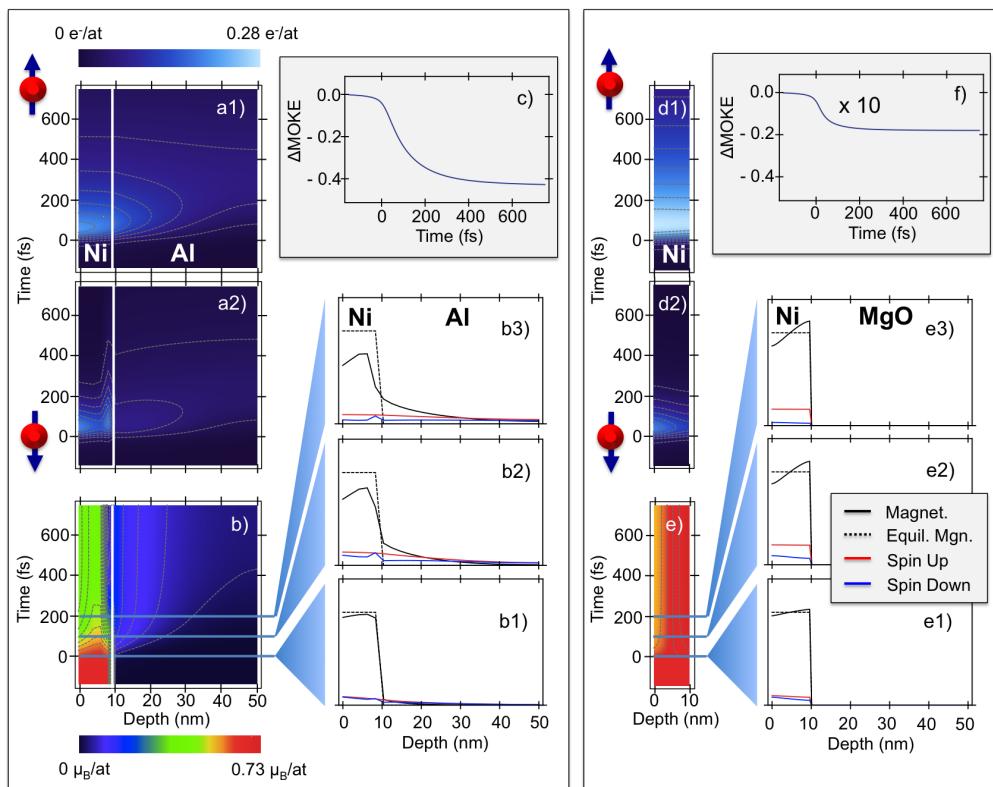
Figure 5.11: Comparison of ultrafast laser-induced spin-dynamics in Ni on different substrates. Panels on the left: the case of 10 nm of Ni on Al. Panels on the right: the case of a 10-nm Ni film on an insulating substrate like MgO. For each case, following the panels in a counterclockwise order and starting from the one at the top left corner, we show the majority-spin electron density, the minority-spin electron density, the magnetization density, three snapshots at three different times and, finally, the normalized MOKE signal change (top-right panel). Reprinted figure from [A.20].

5.3.1 Non-collinear spin structures

In noncollinear systems spin currents can generate spin-transfer torques (STT). Similarly to the problems discussed in Chap. 4, the simplest design to observe this effect represents spin valves consisting of two non-collinear oriented magnetic layers, FM1 and FM2, separated by a nonmagnetic one, NM. If we combine the knowledge about STT with the possibility to create spin currents by an ultrashort laser pulse, it is possible to achieve spin manipulation at femtosecond timescale and generated spin pulses are also localized on the scale of several nm.

We chose the most simple way, assuming the presence of two perpendicular magnetic orientation (Fig. 5.13), which is sufficient to catch all the most important physics. Nevertheless the existing model had to be extended, especially to treat the region between FM layers, where electrons with both spin directions are present. Notable, there are several reasons why this problem is different from the field-driven STT and in fact more complex: In LISC the most important role is played by hot electrons, and it is therefore needed to keep track of the number of excited electrons and their energy for each possible spin state. Another important point is the generally shorter lifetime of these hot electrons compared to those near Fermi
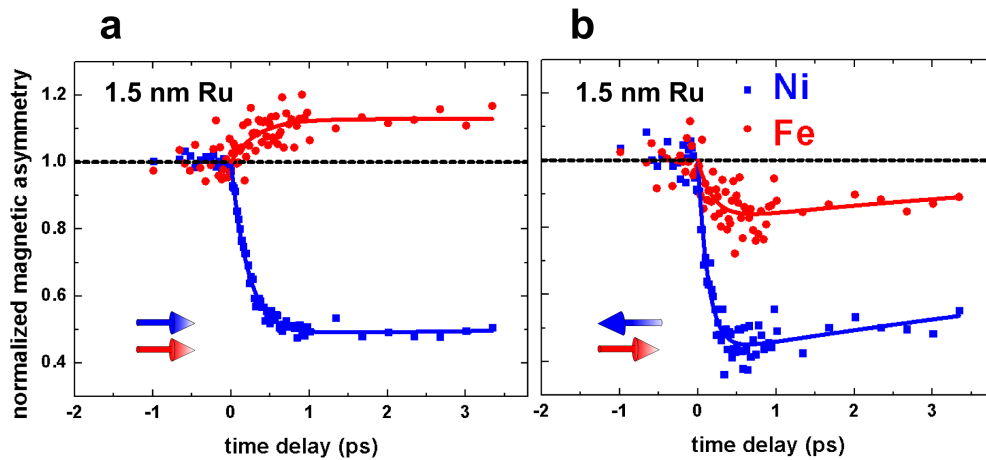
Figure 5.12: Experimentally measured time- and layer-resolved magnetization. The time-resolved magnetization of the Fe and Ni layers in the Ni(5 nm)/Ru(1.5 nm)/Fe(4 nm) trilayer for the parallel (a) and antiparallel (b) magnetization alignment. The magnetic asymmetry at the Fe 3p absorption edge anomalously increases for the parallel (a) and decreases for antiparallel magnetic orientation of Ni and Fe layers (b). Reprinted from [11].

energy, especially in pure metals. Not only a transversal change of magnetization due to STT is possible here, but also a longitudinal one. These effects are observed on a different timescale, and have a limited lifetime.

These facts have to be combined with some basic quantum mechanics governing STT. In a ferromagnet the magnetization axis acts as a natural quantization axis and there are solely two spin eigenstates. When simulating transport through a spin valve where all magnetizations in the magnetic layers are collinear the electrons' spins keep their direction and the two-channel model adequately describes also the transport inside the nonmagnetic layer. In this case the spin quantization axis is fixed in the whole system, but generally it does not have to. In systems without a specific spin direction preferred in the Hamiltonian (e.g. through the magnetization axis) there is however no reason why electron spinors should collapse to the two eigenstates of some specific projection of the spin operator. Therefore, in the case of noncollinear spin valves, the spin current inside the nonmagnetic layer is in general a three-dimensional vector in spin space [73]. The quantization axis of electrons in the nonmagnetic layer depends only on the magnetization direction of the FM layer where from the electrons originated. With two different sources of magnetization orientation there are twice more possible electron spin states. If we choose an arbitrary quantization axis (e.g. along the magnetization in one of the adjacent magnetic layers) the transverse (non-diagonal) spin components inside the nonmagnetic layer will be nonzero. We assumed that electrons excited in FM1 or FM2 keep their spin direction also during the transport inside the nonmagnetic layer. Since the magnetizations in the magnetic layers are perpendicular, we used 4 independent channels to simulate the transport in the nonmagnet. As a result, the total spin
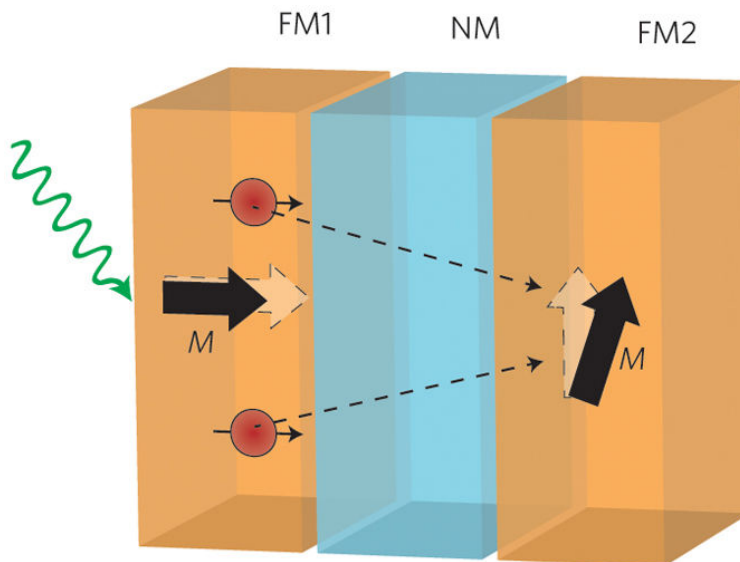
Figure 5.13: Ultrafast spin-transfer torque. When a pump laser hits the first ferromagnetic layer (FM1), which is magnetized in-plane, it induces a demagnetization. A predominantly spin-up electron flow subsequently travels across the interface between FM1 and a non-magnetic layer layer (NM). This generates a net spin current from FM1 to the second ferro-magnetic layer (FM2), which has an out-of-plane magnetization, rotating the magnetization of FM2 [A.21].

current inside the nonmagnetic layer is a sum of 4 spin channels. Assuming short life times of transverse spin components in magnetic layers the model can comprise the description of the whole noncollinear magnetic configuration within its framework. For individual spins it is basically an extension of the superdiffusive model introduced in Sec. 5.3, and any mixing between these spins take place only at interfaces (bulk spin flip scattering is neglected). We have developed and tested a code implementing this generalized model allowing for numerical calculation of spin-transfer torque in ferromagnet-nonmagnet-ferromagnet multilayers driven by laser-excited electrons, where magnetization of the ferromagnetic layers are perpendicular [A.22].

Numerical evaluation of spin currents entering FM2 as a function of basic parameters (laser fluence, layer thickness) with magnetic junction composed from realistic materials (Fe and Cu) leads to interesting conclusions. The calculated dependence on the FM1 thickness (shown in Fig. 5.14) allows us to predict an optimal layer thickness maximizing the exerted torque in the spin valve. We can also evaluate how does the spin current decay with NM thickness (Fig. 5.14). Since the process is accompanied by deexcitation of electrons, this decay is different from a decrease of spin polarization due to spin flips.

Calculated spin transfer torque acting on localized magnetic moments enters the Landau-Lifshitz-Gilbert equation (Eq. 2.3) for the magnetization dynamics and allows us to calculate important quantities (eg. damping of magnetization dynamics, amplitude of magnetization precession), which can be compared directly to experimental results [A.22]. Our first work on this topic assumes macrospin approximation, where the magnetization changes uniformly in the whole FM2 layer. The predicted dynamics is shown in Fig. 5.15.

Without macrospin approximation it is also possible to study the generation of individual
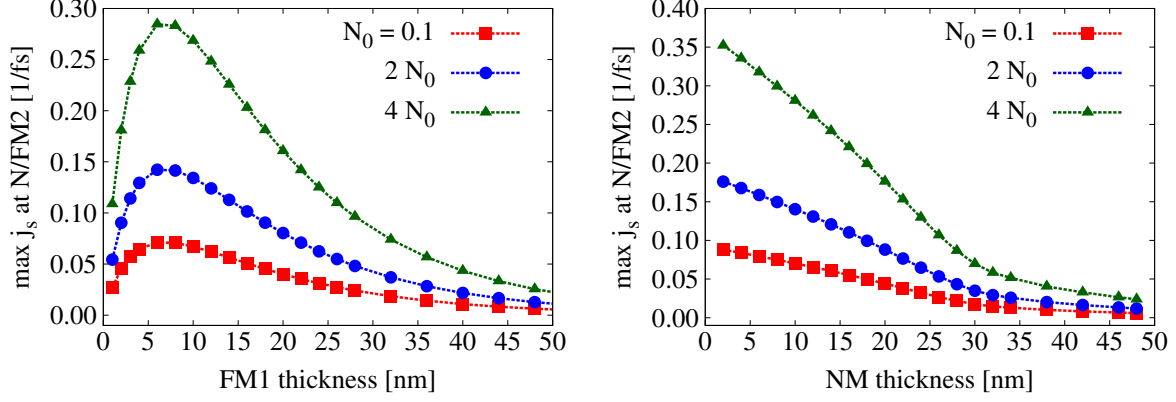
Figure 5.14: Total transverse spin momentum transferred across the NM/FM2 interface transverse to the FM2 magnetization as a function of FM1 thickness (left panel), and as a function of the NM thickness (right panel). The thickness dependence is calculated for three different laser fluences corresponding to $\bar{N}_\sigma(0, \epsilon) = N_0$, $2N_0$, and $3N_0$ [A.22].

excitations in FM2 layer - magnons, since the pulse duration fits within the period of magnons that can exist in typical thin layers employed as FM2, as seen in a recent experiment [125]. This is a unique property of the ultrafast STT driving regime, one cannot expect to see individual magnons when driving STT by an electrical field.

Figure 5.15: Laser-induced magnetization dynamics in the FM2 layer calculated for the trilayer FM1(6)/NM(4)/FM2(6). The solid (red) and dashed (blue) lines are the transverse component of magnetization.

5.4 Opto-magnetic phenomena

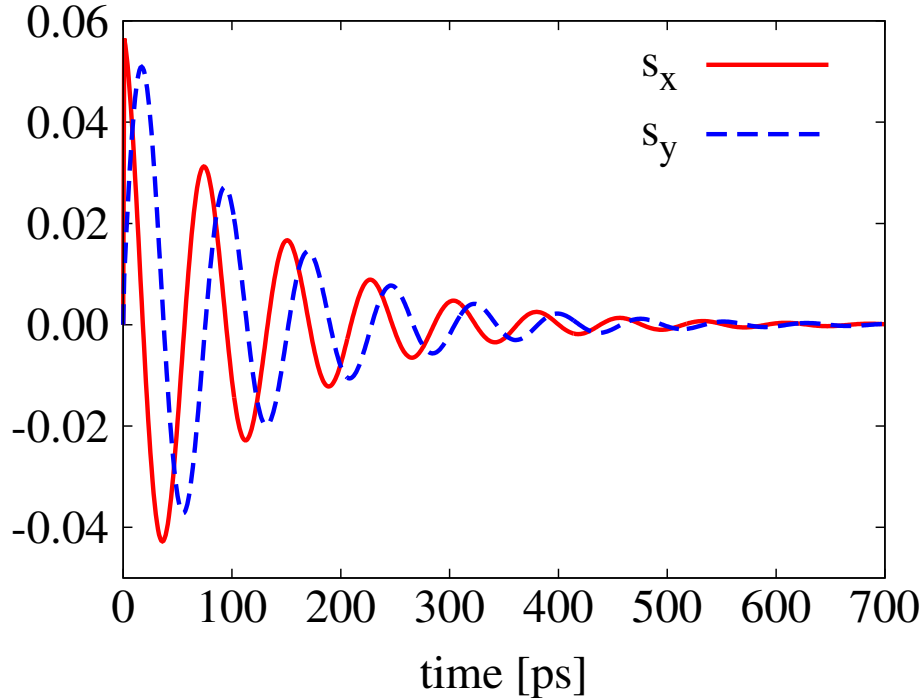Optical pulses can also induce a nonequilibrium magnetization on the femtosecond timescale due to the angular momentum of light, as demonstrated experimentally [126]. Here opposite helicities led to opposite oscillation phases in $DyFeO_3$. This observation has been ascribed to the inverse Faraday effect (IFE), whose theory has originally been derived for paramagnets in a static regime [127, 128]. Note that application of the original theory by Pitaevskii [127] based on the Verdet constant does not provide correct results here by orders of magnitude, also the temperature dependence is not correct [129, 130]. A second order response to an external electromagnetic perturbation has been derived employing the Liouville–von Neumann equation [131]. The final formula for the induced magnetization can be decomposed into three contributions [131] corresponding to:

1. off-diagonal terms in the perturbed density matrix due to the coherence between different levels, which has been induced by the circularly polarized light (corresponds to Raman scattering [132])

2. diagonal elements in the density matrix leading to repopulation of empty levels due to the circularly polarized light

3. another repopulation of levels, representing a static diagonal contribution coming from the part of the response that also leads to the second harmonic generation

The second two effects represent Rayleigh scattering.

We have used this quantum theory to calculate material specific IFE constant from first principles employing the DFT electronic structure [A.23]. This provides the first quantitative predictions of both the spin moment and orbital moment response component for the IFE in the ultrafast regime. For paramagnetic metals (calculated for Cu, Au, Pd and Pt), the small IFE of the spin component competes with that of the orbital component, as these two have opposite sign [A.23]. Here all IFE components are fully antisymmetric w.r.t. photon helicity reversal. In the studied 3d ferromagnets bcc Fe, hcp Co, and fcc Ni the spin component of magnetic response generally dominates over the orbital one or they are comparable (Fig. 5.16). The response is not antisymmetric in the light helicity, its spin component is even invariant to a helicity change. This finding disproves the common assumption of helicity-antisymmetric response in the IFE, and can be relevant for the explanation of a weak helicity dependence observed in GdFeCo alloys [117].

We have also examined the role of spin-orbit interaction (SOI) here, by calculating the response of Fe without SOI. The spin component vanishes without SOI. An orbital contribution is still present, since the L operator does not commute with the Hamiltonian, but its value is strongly reduced compared to the situation with the original value of SOI [A.23].

Optically induced nonequilibrium magnetization has also been observed in semiconductors, it has been ascribed to the optical spin-transfer torque (OSTT, [133]), and the optical spin-orbit torque [134]. The OSTT effect can even initiate domain wall motion [135]. The effect of both IFE and OSTT has recently been calculated using Keldysh nonequilibrium formalism for a different magnetization orientation in metals [136].
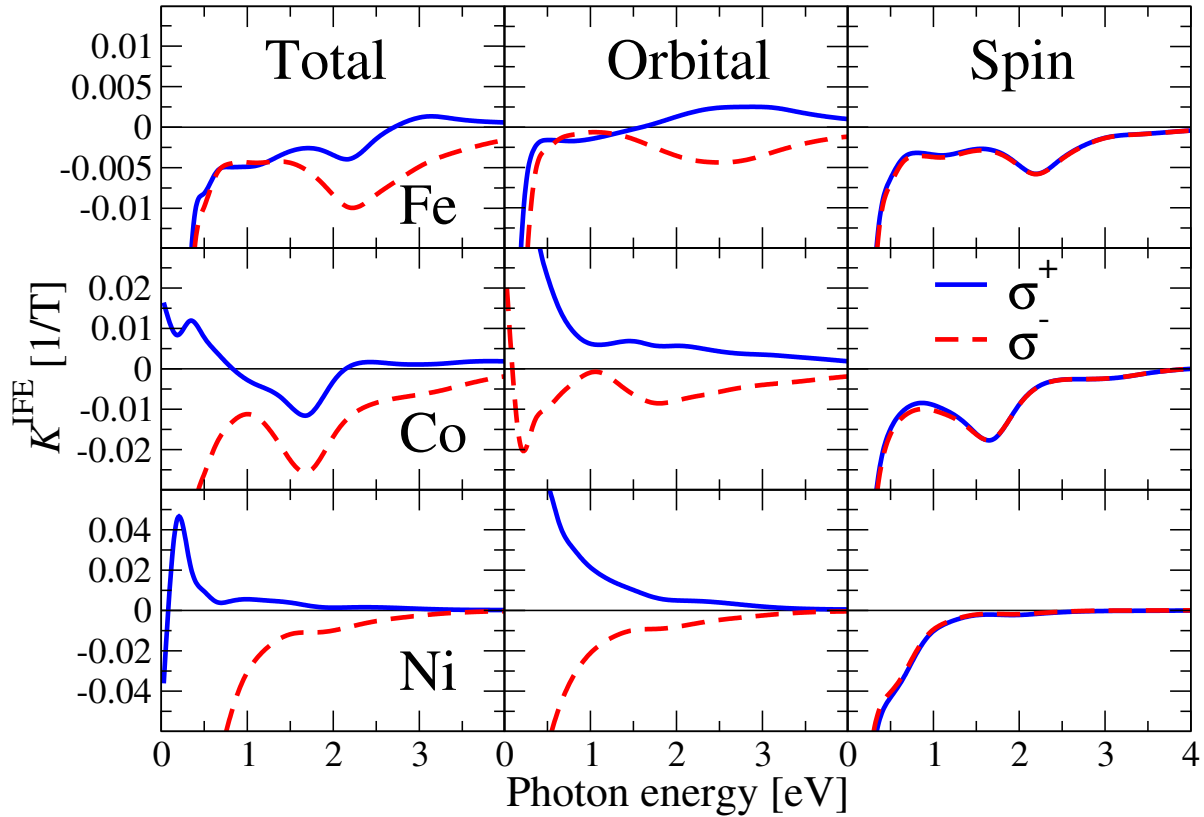
Figure 5.16: (Color online) Calculated total, orbital, and spin inverse Faraday constant $K^{\mathrm{IFE}}(\omega)$ as function of the photon energy and laser polarizations $\sigma^{\pm}$ for ferromagnetic bcc Fe, hcp Co, and fcc Ni. Reprinted figure from [A.23].

5.5   Magneto-optics for transient demagnetized states

Note that magnetization is often probed by magneto-optical (MO) methods. In equilibrium it is possible to assume a linear proportionality between the MO signal (Kerr rotation and ellipticity) and magnetization of the sample. This relation was also assumed in fs demagnetization experiments, however, soon doubts about its applicability arose [137]. We have addressed a similar question related to X-ray absorption spectroscopy (XAS) and X-ray Magnetic Circular Dichroism (XMCD), which is now also used to probe the femtosecond regime [119]. The difference in response between the thermalized and non-thermal electron populations has been studied [A.24]. Similarly to the MO case [98], the XMCD signal has been shown not to be simply proportional to the spin momentum in non-thermal situations, at some energies it decreases and at some it increases. Importantly, the XMCD sum rules for the atomic spin and orbital magnetic moment were found to be valid in the cases studied, even for the laser-induced non-equilibrium electron distributions [A.24]. The question of the MO response has also been addressed in another theoretical work [138], suggesting rules whose satisfaction would guarantee proportionality between the MO response and magnetization. However, only the direct interaction with laser light was considered here, and other flaws of the method were later demonstrated. We have shown that the suggested approach is generally not applicable for fs magnetization dynamics [A.25].

The precise description of the state of demagnetized system on a femtosecond timescale

has been a subject of controversy for long time, and its understanding is clearly important for the above mentioned interpretation of MO experiments. Microscopic theory can predict here relevant relations that cannot be obtained otherwise. Theoretical predictions consider different possible demagnetization scenarios: loss of magnetization due to magnons, reduced local magnetic moment, or high-temperature electronic distribution. Generally the generation of laser induced spin currents (LISC) due to our model for demagnetization (Sec. 5.3) should lead to the second one, the reduced local magnetic moment, and therefore information about this reduction can reveal its role. In collaboration with an experimental group from the University of Colorado we have been able to shed light on this question and resolve the contributions due to these specific processes by combining ultrafast time-, energy-, and angle-resolved measurements of the transverse MOKE at the Co $M_{2,3}$ -absorption edges with advanced ab initio magneto-optical calculations. This study may provide directly answers how big part of magnetization change is responsible for spin current generation. We have shown that the dominant mechanisms contributing to ultrafast demagnetization on time scales up to several picoseconds are a transient reduction of the exchange splitting and the excitation of ultrafast magnons. Surprisingly, the magnon contribution to ultrafast demagnetization is already strong on subpicosecond time scales. On the other hand the reduction of the exchange splitting persists up to several picoseconds, which indicates that the band structure remains modified on this timescale [A.26].

Chapter 6

Conclusions

We have presented here a number of equilibrium and non-equilibrium problems solved using magnetization dynamics, and shown how they help to improve understanding of various observations. First principles microscopic theory has been employed to obtain the local moments and effective interactions, the basic building blocks needed to map real magnetic problems to an effective Heisenberg Hamiltonian. Another important component obtained from microscopic theory is the magnetic anisotropy energy, a subtle effect that rests heavily on relativistic effects. We have shown its sensitivity to the accurate description of relativity as well as to the use of other approximations for the important example of FeCo alloys.

There is a lot of interest in studying magnetization reorientation in CuMnAs, an antiferromagnet with unique features connected to its symmetry. We have demonstrated our ability to describe finite temperature magnetism in this system by predicting correctly critical temperatures of magnetic phase transition. We could also find what defects are present in real samples and how they affect phase stability of this material. Notably, the agreement between theory and experiment confirms that the overall theoretical description and the employed ab initio methods are valid for such system. We have also shown how magnetization dynamics method can be used for dilute magnetic systems and what difficulties appear there.

The effect of spin-polarized current on magnetization is another highly interesting topic where microscopic theory methods can be used. First of all we have derived several important formulas that express the torques exerted on spin in terms of Green functions. This allows to calculate such torque by means of existing electronic structure methods. We have used this method to study several systems and found interesting oscillations of this torque in Ni-based heterostructures, which we linked to the Fermi surface properties. Already a very small amount of disorder in the form of alloying inside the ferromagnetic part can destroy these oscillations, and generally for all studied systems it turns the torque into its most simple form, where all incoming spin current is absorbed. We have also found conditions that lead to an increase of the less common out-of-plane component of this torque.

Especially challenging are findings that touch the timescale where many of our commonly used methods are not valid. In the field of ultrafast magnetization dynamics one of the long-debated problems was the role of phonons in ultrafast demagnetization. Here our calculations have shown that its contribution to demagnetization is rather limited. Furthermore, in collaboration with experiment we have demonstrated that the phononic system remains out of equilibrium for tens of ps, a relatively long time for processes where most important changes take place within 1ps. Femtosecond lasers have also been used to study rare earth systems, where there are two qualitatively different contributions to magnetism: weakly

interacting $4f$ electrons with large momentum, and strongly interacting valence electrons with small momentum. In equilibrium valence momentum is almost completely dependent on $4f$ magnetization, which basically generates it, and can thus be described in a simplified manner. Here we have proposed a model studying magnetization dynamics of these orbital contributions separately, which has been shown to reproduce the experimental observations very well. This shows that on short timescales valence momentum can survive significant deviations from its ground state configuration dictated by $4f$ states. Overall an interesting physical behavior standing between the Heisenberg and Stoner model is revealed here.

Furthermore we have constructed a model studying spin transport induced by femtosecond lasers in ferromagnets. This represents a possible driving mechanism of demagnetization, but also an important source of spin current on an ultrafast timescale, basically generating the sought-after THz pulses. The model has been thoroughly tested for different setups. We have also examined generation of spin-transfer torque in junctions composed of two ferromagnets by means of this effect, and predicted how its magnitude can be affected by the junction geometry.

Finally we have seen that microscopic theories can provide invaluable contributions regarding the optically induced magnetization based on the inverse Faraday effect in the ultrafast regime, where attempts to apply phenomenological approaches have failed. And in the field of direct interaction between light and magnetism on a fs scale first principles calculations are useful in interpreting experimental data, since its interpretation may not be as clear as in equilibrium.

Overall I hope that the works presented in this thesis have contributed significantly to microscopic understanding of a number of challenging open problems from magnetization dynamics.

Bibliography

[1] R. F. L. Evans, W. J. Fan, P. Chureemart, T. A. Ostler, M. O. A. Ellis, and R. W. Chantrell, "Atomistic spin model simulations of magnetic nanomaterials", *J. Phys.: Condens. Matter* **26**, 103202 (2014).

[2] O. Eriksson, A. Bergman, L. Bergqvist, and J. Hellsvik, *Atomistic Spin Dynamics: Foundations and Applications* (OUP Oxford, 2017).

[3] P. Hohenberg and W. Kohn, *Phys. Rev.* **136**, B864 (1964).

[4] W. Kohn and L. J. Sham, *Phys. Rev.* **140**, A1133 (1965).

[5] A. I. Liechtenstein, M. I. Katsnelson, V. P. Antropov, and V. A. Gubanov, *J. Magn. Magn. Mater.* **67**, 65 (1987).

[6] V. P. Antropov, B. N. Harmon, and A. N. Smirnov, *J. Magn. Magn. Mater.* **200**, 148 (1999).

[7] E. Beaurepaire, J.-C. Merle, A. Daunois, and J.-Y. Bigot, "Ultrafast Spin Dynamics in Ferromagnetic Nickel", *Phys. Rev. Lett.* **76**, 4250– (1996).

[8] A. Einstein, "Experimenteller Nachweis der Ampereschen Molekularstrome", *Verh. d. Deutsch. Phy. Ges.*, 152–170 (1915).

[9] A. Kirilyuk, A. V. Kimel, and T. Rasing, "Ultrafast optical manipulation of magnetic order", *Rev. Mod. Phys.* **82**, 2731– (2010).

[10] I. Radu, K. Vahaplar, C. Stamm, T. Kachel, N. Pontius, H. A. Durr, T. A. Ostler, J. Barker, R. F. L. Evans, R. W. Chantrell, et al., "Transient ferromagnetic-like state mediating ultrafast reversal of antiferromagnetically coupled spins", *Nature* **472**, 205–208 (2011).

[11] D. Rudolf, C. La-O-Vorakiat, M. Battiato, R. Adam, J. M. Shaw, E. Turgut, P. Maldonado, S. Mathias, P. Grychtol, H. T. Nembach, et al., "Ultrafast magnetization enhancement in metallic multilayers driven by superdiffusive spin current", *Nat Commun* **3**, 1037 (2012).

[12] E. Ising, "Beitrag zur Theorie des Ferromagnetismus", *Zeitschrift für Physik* **31**, 253–258 (1925).

[13] V. P. Antropov, M. I. Katsnelson, M. van Schilfgaarde, and B. N. Harmon, "Ab Initio Spin Dynamics in Magnets", *Phys. Rev. Lett.* **75**, 729–732 (1995).

[14] M. Stamenova and S. Sanvito, "Dynamical exchange interaction from time-dependent spin density functional theory", *Phys. Rev. B* **88**, 104423 (2013).

[15] K. Krieger, J. K. Dewhurst, P. Elliott, S. Sharma, and E. K. U. Gross, "Laser-Induced Demagnetization at Ultrashort Time Scales: Predictions of TDDFT", *Journal of Chemical Theory and Computation* **11**, 4870–4874 (2015).

[16] P. Elliott, K. Krieger, J. K. Dewhurst, S. Sharma, and E. K. U. Gross, "Optimal control of laser-induced spin–orbit mediated ultrafast demagnetization", *New J. Phys.* **18**, 013014 (2016).

[17] K. Krieger, P. Elliott, T. Müller, N. Singh, J. K. Dewhurst, E. K. U. Gross, and S. Sharma, "Ultrafast demagnetization in bulk versus thin films: an ab initio study", *J. Phys.: Condens. Matter* **29**, 224001 (2017).

[18] A. I. Liechtenstein, M. I. Katsnelson, and V. A. Gubanov, "Exchange interactions and spin-wave stiffness in ferromagnetic metals", *Journal of Physics F: Metal Physics* **14**, L125– (1984).

[19] S. V. Halilov, A. Y. Perlov, P. M. Oppeneer, and H. Eschrig, "Magnon spectrum and related finite-temperature magnetic properties: A first-principle approach", *EPL (Europhysics Letters)* **39**, 91– (1997).

[20] M. Šob, "The role of ab initio electronic structure calculations in multiscale modelling of materials", in *Multiscale Materials Modelling* (Elsevier, 2007), pp. 1–24.

[21] R. E. Watson, M. Blume, and G. H. Vineyard, "Spin Motions in a Classical Ferromagnet", *Physical Review* **181**, 811–823 (1969).

[22] I. Turek, V. Drchal, J. Kudrnovský, M. Šob, and P. Weinberger, *Electronic Structure of Disordered Alloys, Surfaces and Interfaces* (Kluwer, Boston, 1997).

[23] I. Turek, J. Kudrnovský, V. Drchal, and P. Bruno, "Exchange interactions, spin waves, and transition temperatures in itinerant magnets", *Philosophical Magazine* **86**, 1713–1752 (2006).

[24] M. Zelený, D. Legut, and M. Šob, "Ab initio study of Co and Ni under uniaxial and biaxial loading and in epitaxial overlayers", *Phys. Rev. B* **78**, 224105 (2008).

[25] M. Zelený, M. Friák, and M. Šob, "Ab initio study of energetics and magnetism of Fe, Co, and Ni along the trigonal deformation path", *Phys. Rev. B* **83**, 184424 (2011).

[26] P. Buczek, A. Ernst, and L. M. Sandratskii, "Different dimensionality trends in the Landau damping of magnons in iron, cobalt, and nickel: Time-dependent density functional study", *Phys. Rev. B* **84**, 174418 (2011).

[27] B. L. Gyorffy, A. J. Pindor, J. Staunton, G. M. Stocks, and H. Winter, "A first-principles theory of ferromagnetic phase transitions in metals", *Journal of Physics F: Metal Physics* **15**, 1337 (1985).

[28] J. Kudrnovský, V. Drchal, I. Turek, S. Khmelevskyi, J. K. Glasbrenner, and K. D. Belashchenko, "Spin-disorder resistivity of ferromagnetic metals from first principles: The disordered-local-moment approach", *Phys. Rev. B* **86**, 144423 (2012).

[29] R. Chimata, A. Bergman, L. Bergqvist, B. Sanyal, and O. Eriksson, "Microscopic Model for Ultrafast Remagnetization Dynamics", *Phys. Rev. Lett.* **109**, 157201– (2012).

[30] B. Velický, S. Kirkpatrick, and H. Ehrenreich, *Phys. Rev.* **175**, 747 (1968).

[31] J. Kudrnovský, I. Turek, V. Drchal, F. Máca, J. Mašek, P. Weinberger, and P. Bruno, "Ab Initio Study of Curie Temperatures of Diluted Magnetic Semiconductors", *J. Superconductivity* **16**, 119 (2003).

[32] M. Friák, A. Slávik, I. Miháliková, D. Holec, M. Všianská, M. Šob, M. Palm, and J. Neugebauer, "Origin of the Low Magnetic Moment in Fe2AlTi: An Ab Initio Study", *Materials* **11**, 1732 (2018).

[33] L. D. Landau and E. Lifshitz, "On the theory of the dispersion of magnetic permeability in ferromagnetic bodies", *Phys. Z. Sowjet.* **8**, 153 (1935).

[34] T. L. Gilbert, "A phenomenological theory of damping in ferromagnetic materials", *IEEE Trans. Magn.* **40**, 3443–3449 (2004).

[35] V. Kamberský, "On ferromagnetic resonance damping in metals", *Czech. J. Phys. B* **26**, 1366–1383 (1976).

[36] V. Kamberský, "Spin-orbital Gilbert damping in common magnetic metals", *Phys. Rev. B* **76**, 134416–10 (2007).

[37] A. A. Starikov, P. J. Kelly, A. Brataas, Y. Tserkovnyak, and G. E. W. Bauer, "Unified First-Principles Study of Gilbert Damping, Spin-Flip Diffusion, and Resistivity in Transition Metal Alloys", *Phys. Rev. Lett.* **105**, 236601– (2010).

[38] I. Turek, J. Kudrnovský, and V. Drchal, "Nonlocal torque operators in ab initio theory of the Gilbert damping in random ferromagnetic alloys", *Phys. Rev. B* **92**, 214407 (2015).

[39] W. F. Brown, "Thermal Fluctuations of a Single-Domain Particle", *Phys. Rev.* **130**, 1677–1686 (1963).

[40] W. Scholz, T. Schrefl, and J. Fidler, "Micromagnetic simulation of thermally activated switching in fine particles", *J. Magn. Magn. Mater.* **233**, 296–304 (2001).

[41] B. Skubic, J. Hellsvik, L. Nordström, and O. Eriksson, "A method for atomistic spin dynamics simulations: implementation and examples", *J. Phys.: Condens. Matter* **20**, 315203 (2008).

[42] J. Hellsvik, B. Skubic, L. Nordström, B. Sanyal, O. Eriksson, P. Nordblad, and P. Svedlindh, "Dynamics of diluted magnetic semiconductors from atomistic spin-dynamics simulations: Mn-doped GaAs", *Phys. Rev. B* **78**, 144419 (2008).

[43] D. A. Garanin and O. Chubykalo-Fesenko, "Thermal fluctuations and longitudinal relaxation of single-domain magnetic particles at elevated temperatures", *Phys. Rev. B* **70**, 212409 (2004).

[44] J. Trygg, B. Johansson, O. Eriksson, and J. M. Wills, "Total Energy Calculation of the Magnetocrystalline Anisotropy Energy in the Ferromagnetic 3d Metals", *Phys. Rev. Lett.* **75**, 2871–2874 (1995).

[45] S. V. Halilov, A. Y. Perlov, P. M. Oppeneer, A. N. Yaresko, and V. N. Antonov, "Magnetocrystalline anisotropy energy in cubic Fe, Co, and Ni: Applicability of local-spin-density theory reexamined", *Phys. Rev. B* **57**, 9557–9560 (1998).

[46] A. B. Shick, S. Khmelevskyi, O. N. Mryasov, J. Wunderlich, and T. Jungwirth, "Spin-orbit coupling induced anisotropy effects in bimetallic antiferromagnets: A route towards antiferromagnetic spintronics", *Phys. Rev. B* **81**, 212409– (2010).

[47] X. Marti, I. Fina, C. Frontera, J. Liu, P. Wadley, Q. He, R. J. Paull, J. D. Clarkson, J. Kudrnovsky J., I. Turek, et al., "Room-temperature antiferromagnetic memory resistor", *Nat Mater* **13**, 367–374 (2014).

[48] A. A. Khajetoorians, M. Valentyuk, M. Steinbrecher, T. Schlenk, A. Shick, J. Kolorenc, A. I. Lichtenstein, T. O. Wehling, R. Wiesendanger, and J. Wiebe, "Tuning emergent magnetism in a Hund's impurity", *Nat. Nanotechnol.* **10**, 958–964 (2015).

[49] T. Burkert, L. Nordstrom, O. Eriksson, and O. Heinonen, "Giant Magnetic Anisotropy in Tetragonal FeCo Alloys", *Phys. Rev. Lett.* **93**, 027203– (2004).

[50] F. Yildiz, M. Przybylski, X.-D. Ma, and J. Kirschner, "Strong perpendicular anisotropy in $Fe_{1-x}Co_x$ alloy films epitaxially grown on mismatching Pd(001), Ir(001), and Rh(001) substrates", *Phys. Rev. B* **80**, 064415– (2009).

[51] J. Li, M. Przybylski, F. Yildiz, X. D. Ma, and Y. Z. Wu, "Oscillatory Magnetic Anisotropy Originating from Quantum Well States in Fe Films", *Phys. Rev. Lett.* **102**, 207206– (2009).

[52] P. Bruno, "Tight-binding approach to the orbital magnetic moment and magnetocrystalline anisotropy of transition-metal monolayers", *Phys. Rev. B* **39**, 865–868 (1989).

[53] L. Reichel, G. Giannopoulos, S. Kauffmann-Weiss, M. Hoffmann, D. Pohl, A. Edström, S. Oswald, D. Niarchos, J. Rusz, L. Schultz, et al., "Increased magnetocrystalline anisotropy in epitaxial Fe-Co-C thin films with spontaneous strain", *Journal of Applied Physics* **116**, 213901 (2014) http://dx.doi.org/10.1063/1.4901595.

[54] M. Werwiński, A. Edström, J. Rusz, D. Hedlund, K. Gunnarsson, P. Svedlindh, J. Cedervall, and M. Sahlberg, "Magnetocrystalline anisotropy of Fe5PB2 and its alloys with Co and 5d elements: A combined first-principles and experimental study", *Phys. Rev. B* **98** (2018) 10.1103/physrevb.98.214431.

[55] S. Khmelevskyi, J. Kudrnovský, B. L. Gyorffy, P. Mohn, V. Drchal, and P. Weinberger, "Frustration and long-range behavior of the exchange interactions in AuFe spin-glass alloys", *Phys. Rev. B* **70**, 224432 (2004).

[56] N. Metropolis, A. W. Rosenbluth, M. N. Rosenbluth, A. H. Teller, and E. Teller, "Equation of State Calculations by Fast Computing Machines", *The Journal of Chemical Physics* **21**, 1087–1092 (1953).

[57] D. Hinzke and U. Nowak, "Monte Carlo simulation of magnetization switching in a Heisenberg model for small ferromagnetic particles", *Computer Physics Communications* **121-122**, 334–337 (1999).

[58] K. Binder, "Finite size scaling analysis of ising model block distribution functions", *Zeit. Phys. B Cond. Mat.* **43**, 119–140 (1981).

[59] D. Kriegner, K. Výborný, K. Olejník, H. Reichlová, V. Novák, X. Marti, J. Gazquez, V. Saidl, P. Němec, V. V. Volobuev, et al., "Multiple-stable anisotropic magnetoresistance memory in antiferromagnetic MnTe", *Nat. Commun.* **7**, 11623 (2016).

[60] K. Olejník, V. Schuler, X. Marti, V. Novák, Z. Kašpar, P. Wadley, R. P. Campion, K. W. Edmonds, B. L. Gallagher, J. Garces, et al., "Antiferromagnetic CuMnAs multi-level memory cell with microelectronic compatibility", *Nat. Commun.* **8**, 15434 (2017).

[61] P. Wadley, B. Howells, J. Železný, C. Andrews, V. Hills, R. P. Campion, V. Novák, K. Olejník, F. Maccherozzi, S. S. Dhesi, et al., "Electrical switching of an antiferromagnet", *Science* **351**, 587–590 (2016).

[62] K. Uhlířová, E. Duverger-Nédellec, R. H. Colman, J. Volný, B. Vondráčková, and K. Carva, "The stability and physical properties of the tetragonal phase of bulk CuMnAs antiferromagnet", *J. Alloys Compd.* **771**, 680–685 (2019).

[63] M. Veis, J. Minár, G. Steciuk, L. Palatinus, C. Rinaldi, M. Cantoni, D. Kriegner, K. K. Tikuišis, J. Hamrle, M. Zahradník, et al., "Band structure of CuMnAs probed by optical and photoemission spectroscopy", *Phys. Rev. B* **97**, 125109 (2018).

[64] G. Kresse and D. Joubert, "From ultrasoft pseudopotentials to the projector augmented-wave method", *Phys. Rev. B* **59**, 1758–1775 (1999).

[65] C. Datzer, A. Zumbülte, J. Braun, T. Förster, A. B. Schmidt, J. Mi, B. Iversen, P. Hofmann, J. Minár, H. Ebert, et al., "Unraveling the spin structure of unoccupied states in Bi_2Se_3", *Phys. Rev. B* **95**, 115401 (2017).

[66] M. Z. Hasan and C. L. Kane, "*Colloquium* : Topological insulators", *Rev. Mod. Phys.* **82**, 3045–3067 (2010).

[67] Y. S. Hor, P. Roushan, H. Beidenkopf, J. Seo, D. Qu, J. G. Checkelsky, L. A. Wray, D. Hsieh, Y. Xia, S.-Y. Xu, et al., "Development of ferromagnetism in the doped topological insulator $Bi_{2-x}Mn_xTe_3$", *Phys. Rev. B* **81**, 195203 (2010).

[68] J. Sanchez-Barriga, A. Varykhalov, G. Springholz, H. Steiner, R. Kirchschlager, G. Bauer, O. Caha, E. Schierle, E. Weschke, A. A. Unal, et al., "Nonmagnetic band gap at the Dirac point of the magnetic topological insulator (Bi1-xMnx)2Se3", *Nat Commun* **7**, – (2016).

[69] H. J. von Bardeleben, J. L. Cantin, D. M. Zhang, A. Richardella, D. W. Rench, N. Samarth, and J. A. Borchers, "Ferromagnetism in Bi_2Se_3:Mn epitaxial layers", *Phys. Rev. B* **88**, 075149 (2013).

[70] V. Maurya, C. Dong, C. Chen, K. Asokan, and S. Patnaik, "High spin state driven magnetism and thermoelectricity in Mn doped topological insulator Bi2Se3", *J. Magn. Magn. Mater.* **456**, 1–5 (2018).

[71] P. Janíček, Č. Drašar, P. Lošt'ák, J. Vejpravová, and V. Sechovský, "Transport, magnetic, optical and thermodynamic properties of Bi2-xMnxSe3 single crystals", *Physica B* **403**, 3553–3558 (2008).

[72] J. C. Slonczewski, *J. Magn. Magn. Mater.* **159**, L1 (1996).

[73] M. D. Stiles and A. Zangwill, "Anatomy of spin-transfer torque", *Phys. Rev. B* **66**, 014407 (2002).

[74] Y. K. Kato, R. C. Myers, A. C. Gossard, and D. D. Awschalom, "Observation of the Spin Hall Effect in Semiconductors", *Science* **306**, 1910–1913 (2004).

[75] T. Jungwirth, J. Wunderlich, and K. Olejnik, "Spin Hall effect devices", *Nat Mater* **11**, 382–390 (2012).

[76] A. Manchon and S. Zhang, "Theory of spin torque due to spin-orbit coupling", *Phys. Rev. B* **79**, 094422– (2009).

[77] D. Fang, H. Kurebayashi, J. Wunderlich, K. Výborný, L. P. Zârbo, R. P. Campion, A. Casiraghi, B. L. Gallagher, T. Jungwirth, and A. J. Ferguson, "Spin-orbit-driven ferromagnetic resonance", *Nat Nano* **6**, 413–417 (2011).

[78] J. Železný, H. Gao, K. Výborný, J. Zemen, J. Mašek, A. Manchon, J. Wunderlich, J. Sinova, and T. Jungwirth, "Relativistic Néel-Order Fields Induced by Electrical Current in Antiferromagnets", *Phys. Rev. Lett.* **113**, 157201– (2014).

[79] T. Jungwirth, X. Marti, P. Wadley, and J. Wunderlich, "Antiferromagnetic spintronics", *Nat Nano* **11**, 231–241 (2016).

[80] J. Sinova, S. O. Valenzuela, J. Wunderlich, C. H. Back, and T. Jungwirth, "Spin Hall effects", *Rev. Mod. Phys.* **87**, 1213–1260 (2015).

[81] S. Y. Bodnar, L. Šmejkal, I. Turek, T. Jungwirth, O. Gomonay, J. Sinova, A. A. Sapozhnik, H.-J. Elmers, M. Kläui, and M. Jourdan, "Writing and reading antiferromagnetic Mn 2 Au by Néel spin-orbit torques and large anisotropic magnetoresistance", *Nat. Commun.* **9**, 348 (2018).

[82] A. Brataas, Y. V. Nazarov, and G. E. W. Bauer, "Finite-Element Theory of Transport in Ferromagnet–Normal Metal Systems", *Phys. Rev. Lett.* **84**, 2481 (2000).

[83] A. Brataas, Y. V. Nazarov, and G. E. W. Bauer, *Euro. Phys. J. B* **22**, 99 (2001).

[84] A. Brataas, G. E. W. Bauer, and P. J. Kelly, "Non-collinear magnetoelectronics", *Phys. Rep.* **427**, 157 (2006).

[85] K. Xia, P. J. Kelly, G. E. W. Bauer, A. Brataas, and I. Turek, *Phys. Rev. B* **65**, 220401(R) (2002).

[86] S. Datta, *Electronic Transport in Mesoscopic Systems* (Cambridge University Press, Cambridge, 1995).

[87] I. Turek and K. Carva, "Spin-mixing conductances of metallic and half-metallic magnetic layers", *J. Phys.: Condens. Matter* **19**, 365203 (2007).

[88] T. Valet and A. Fert, *Phys. Rev. B* **48**, 7099 (1993).

[89] K. Carva and I. Turek, "Bulk and epitaxial Co_2MnSi: Ab Initio Calculations", *Acta Phys. Pol.* **113**, 183 (2008).

[90] C. Dornes, Y. Acremann, M. Savoini, M. Kubli, M. J. Neugebauer, E. Abreu, L. Huber, G. Lantz, C. A. F. Vaz, H. Lemke, et al., "The ultrafast Einstein–de Haas effect", *Nature* **565**, 209–212 (2019).

[91] D. A. Garanin and E. M. Chudnovsky, "Angular momentum in spin-phonon processes", *Phys. Rev. B* **92**, 024421 (2015).

[92] R. J. Elliott, "Theory of the Effect of Spin-Orbit Coupling on Magnetic Resonance in Some Semiconductors", *Phys. Rev.* **96**, 266– (1954).

[93] B. Koopmans, H. Kicken, M. van Kampen, and W. de Jonge, "Microscopic model for femtosecond magnetization dynamics", *J. Magn. Magn. Mater.* **286**, 271–275 (2005).

[94] B. Koopmans, J. J. M. Ruigrok, F. D. Longa, and W. J. M. de Jonge, "Unifying Ultrafast Magnetization Dynamics", *Phys. Rev. Lett.* **95**, 267207–4 (2005).

[95] B. Koopmans, G. Malinowski, F. Dalla Longa, D. Steiauf, M. Fahnle, T. Roth, M. Cinchetti, and M. Aeschlimann, "Explaining the paradoxical diversity of ultrafast laser-induced demagnetization", *Nat Mater* **9**, 259–265 (2010).

[96] J. Fabian and S. Das Sarma, "Spin Relaxation of Conduction Electrons in Polyvalent Metals: Theory and a Realistic Calculation", *Phys. Rev. Lett.* **81**, 5624– (1998).

[97] J. Fabian and S. Das Sarma, "Phonon-Induced Spin Relaxation of Conduction Electrons in Aluminum", *Phys. Rev. Lett.* **83**, 1211– (1999).

[98] P. M. Oppeneer and A. Liebsch, "Ultrafast demagnetization in Ni: theory of magneto-optics for non-equilibrium electron distributions", *J. Phys.: Condens. Matter* **16**, 5519–5530 (2004).

[99] D. Steiauf and M. Fähnle, "Elliott-Yafet mechanism and the discussion of femtosecond magnetization dynamics", *Phys. Rev. B* **79**, 140401–3 (2009).

[100] B. Y. Mueller, A. Baral, S. Vollmar, M. Cinchetti, M. Aeschlimann, H. C. Schneider, and B. Rethfeld, "Feedback Effect during Ultrafast Demagnetization Dynamics in Ferromagnets", *Phys. Rev. Lett.* **111**, 167204– (2013).

[101] J. Hellsvik, D. Thonig, K. Modin, D. Iuşan, A. Bergman, O. Eriksson, L. Bergqvist, and A. Delin, "General method for atomistic spin-lattice dynamics with first-principles accuracy", *Phys. Rev. B* **99** (2019) `10.1103/physrevb.99.104302`.

[102] S. Anisimov, B. Kapeliovich, and T. Perelman, "Electron-Emission from Surface of Metals Induced by Ultrashort Laser Pulses", *Zhurnal Eksperimentalnoi I Teoreticheskoi Fiziki* **66**, 776–781 (1974).

[103] T. Henighan, M. Trigo, S. Bonetti, P. Granitzka, D. Higley, Z. Chen, M. P. Jiang, R. Kukreja, A. Gray, A. H. Reid, et al., "Generation mechanism of terahertz coherent acoustic phonons in Fe", *Phys. Rev. B* **93**, 220301 (2016).

[104] L. Waldecker, R. Bertoni, R. Ernstorfer, and J. Vorberger, "Electron-Phonon Coupling and Energy Flow in a Simple Metal beyond the Two-Temperature Approximation", *Phys. Rev. X* **6**, 021003 (2016).

[105] L. Waldecker, R. Bertoni, H. Hübener, T. Brumme, T. Vasileiadis, D. Zahn, A. Rubio, and R. Ernstorfer, "Momentum-Resolved View of Electron-Phonon Coupling in Multilayer WSe_2", *Phys. Rev. Lett.* **119**, 036803 (2017).

[106] P. Kurz, G. Bihlmayer, and S. Blugel, "Magnetism and electronic structure of hcp Gd and the Gd(0001) surface", *J. Phys.: Condens. Matter* **14**, 6353–6371 (2002).

[107] A. L. Kozub, A. B. Shick, F. Máca, J. Kolorenč, and A. I. Lichtenstein, "Electronic structure and magnetism of samarium and neodymium adatoms on free-standing graphene", *Phys. Rev. B* **94**, 125113 (2016).

[108] S. Khmelevskyi, I. Turek, and P. Mohn, "Spontaneous volume magnetostriction and non-Stoner behavior of the valence band in pure hcp Gd", *Phys. Rev. B* **70**, 132401 (2004).

[109] I. Turek, J. Kudrnovský, G. Bihlmayer, and S. Blügel, *J. Phys.: Condens. Matter* **15**, 2771 (2003).

[110] B. Kim, A. B. Andrews, J. L. Erskine, K. J. Kim, and B. N. Harmon, "Temperature-dependent conduction-band exchange splitting in ferromagnetic hcp gadolinium: Theoretical predictions and photoemission experiments", *Phys. Rev. Lett.* **68**, 1931–1934 (1992).

[111] M. Donath, B. Gubanka, and F. Passek, "Temperature-Dependent Spin Polarization of Magnetic Surface State at Gd(0001)", *Phys. Rev. Lett.* **77**, 5138–5141 (1996).

[112] L. M. Sandratskii and J. Kübler, "Local Magnetic Moments of Conduction Electrons in Gadolinium", *Europhysics Letters (EPL)* **23**, 661–666 (1993).

[113] K. Maiti, M. C. Malagoli, A. Dallmeyer, and C. Carbone, "Finite Temperature Magnetism in Gd: Evidence against a Stoner Behavior", *Phys. Rev. Lett.* **88**, 167205– (2002).

[114] L. M. Sandratskii, "Exchange splitting of surface and bulk electronic states in excited magnetic states of Gd: First-principles study", *Phys. Rev. B* **90**, 184406 (2014).

[115] J. Seib and M. Fahnle, "Calculation of the Gilbert damping matrix at low scattering rates in Gd", *Phys. Rev. B* **82**, 064401– (2010).

[116] C. D. Stanciu, F. Hansteen, A. V. Kimel, A. Kirilyuk, A. Tsukamoto, A. Itoh, and T. Rasing, "All-Optical Magnetic Recording with Circularly Polarized Light", *Phys. Rev. Lett.* **99**, 047601–4 (2007).

[117] T. Ostler, J. Barker, R. Evans, R. Chantrell, U. Atxitia, O. Chubykalo-Fesenko, S. El Moussaoui, L. Le Guyader, E. Mengotti, L. Heyderman, et al., "Ultrafast heating as a sufficient stimulus for magnetization reversal in a ferrimagnet", *Nat Commun* **3**, 666– (2012).

[118] V. P. Zhukov, E. V. Chulkov, and P. M. Echenique, "GW+T theory of excited electron lifetimes in metals", *Phys. Rev. B* **72**, 155109– (2005).

[119] C. Stamm, T. Kachel, N. Pontius, R. Mitzner, T. Quast, K. Holldack, S. Khan, C. Lupulescu, E. F. Aziz, M. Wietstruk, et al., "Femtosecond modification of electron localization and transfer of angular momentum in nickel", *Nat. Mater.* **6**, 740–743 (2007).

[120] M. Battiato, P. Maldonado, and P. M. Oppeneer, "Treating the effect of interface reflections on superdiffusive spin transport in multilayer samples (invited)", *Journal of Applied Physics* **115**, 172611 (2014).

[121] B. Pfau, S. Schaffert, L. Müller, C. Gutt, A. Al-Shemmary, F. Büttner, R. Delaunay, S. Düsterer, S. Flewett, R. Frömter, et al., "Ultrafast optical demagnetization manipulates nanoscale spin structure in domain walls", *Nat Commun* **3**, 1100 (2012).

[122] E. Turgut, C. La-o-vorakiat, J. M. Shaw, P. Grychtol, H. T. Nembach, D. Rudolf, R. Adam, M. Aeschlimann, C. M. Schneider, T. J. Silva, et al., "Controlling the Competition between Optically Induced Ultrafast Spin-Flip Scattering and Spin Transport in Magnetic Multilayers", *Phys. Rev. Lett.* **110**, 197201– (2013).

[123] A. Eschenlohr, M. Battiato, P. Maldonado, N. Pontius, T. Kachel, K. Holldack, R. Mitzner, A. Fohlisch, P. M. Oppeneer, and C. Stamm, "Ultrafast spin transport as key to femtosecond demagnetization", *Nat Mater* **12**, 332–336 (2013).

[124] T. Kampfrath, M. Battiato, P. Maldonado, EilersG., NotzoldJ., MahrleinS., ZbarskyV., FreimuthF., Y. Mokrousov, S. Blugel, et al., "Terahertz spin current pulses controlled by magnetic heterostructures", *Nat Nano* **8**, 256–260 (2013).

[125] I. Razdolski, A. Alekhin, N. Ilin, J. P. Meyburg, V. Roddatis, D. Diesing, U. Bovensiepen, and A. Melnikov, "Nanoscale interface confinement of ultrafast spin transfer torque driving non-uniform spin dynamics", *Nat. Commun.* **8**, 15007 (2017).

[126] A. V. Kimel, A. Kirilyuk, P. A. Usachev, R. V. Pisarev, A. M. Balbashov, and T. Rasing, "Ultrafast non-thermal control of magnetization by instantaneous photomagnetic pulses", *Nature* **435**, 655–657 (2005).

[127] L. Pitaevskii, "Electric Forces in a Transparent Dispersive Medium", *Soviet Physics Jetp-Ussr* **12**, 1008–1013 (1961).

[128] J. P. van der Ziel, P. S. Pershan, and L. D. Malmstrom, "Optically-Induced Magnetization Resulting from the Inverse Faraday Effect", *Phys. Rev. Lett.* **15**, 190– (1965).

[129] A. H. M. Reid, A. V. Kimel, A. Kirilyuk, J. F. Gregg, and T. Rasing, "Investigation of the femtosecond inverse Faraday effect using paramagnetic $Dy_3Al_5O_1 2$", *Phys. Rev. B* **81**, 104404 (2010).

[130] R. V. Mikhaylovskiy, E. Hendry, and V. V. Kruglyak, "Ultrafast inverse Faraday effect in a paramagnetic terbium gallium garnet crystal", *Phys. Rev. B* **86**, 100405 (2012).

[131] M. Battiato, G. Barbalinardo, and P. M. Oppeneer, "Quantum theory of the inverse Faraday effect", *Phys. Rev. B* **89**, 014413 (2014).

[132] D. Popova, A. Bringer, and S. Blügel, "Theory of the inverse Faraday effect in view of ultrafast magnetization experiments", *Phys. Rev. B* **84**, 214421 (2011).

[133] P. Němec, E. Rozkotova, N. Tesarova, F. Trojanek, E. De Ranieri, K. Olejnik, J. Zemen, V. Novak, M. Cukr, P. Maly, et al., "Experimental observation of the optical spin transfer torque", *Nat Phys* **8**, 411–415 (2012).

[134] N. Tesařová, P. Němec, E. Rozkotová, J. Zemen, T. Janda, D. Butkovičová, F. Trojánek, K. Olejník, V. Novák, P. Malý, et al., "Experimental observation of the optical spin-orbit torque", *Nat. Photonics* **7**, 492–498 (2013).

[135] T. Janda, P. E. Roy, R. M. Otxoa, Z. Šobáň, A. Ramsay, A. C. Irvine, F. Trojanek, M. Surýnek, R. P. Campion, B. L. Gallagher, et al., "Inertial displacement of a domain wall excited by ultra-short circularly polarized laser pulses", *Nat. Commun.* **8**, 15226 (2017).

[136] F. Freimuth, S. Blügel, and Y. Mokrousov, "Laser-induced torques in metallic ferromagnets", *Phys. Rev. B* **94**, 144432 (2016).

[137] B. Koopmans, M. van Kampen, J. T. Kohlhepp, and W. J. M. de Jonge, "Ultrafast Magneto-Optics in Nickel: Magnetism or Optics?", *Phys. Rev. Lett.* **85**, 844– (2000).

[138] G. P. Zhang, W. Hubner, G. Lefkidis, Y. Bai, and T. F. George, "Paradigm of the time-resolved magneto-optical Kerr effect for femtosecond magnetism", *Nat Phys* **5**, 499 (2009).

List of attached publications

[A.1] D. Hinzke, U. Atxitia, K. Carva, P. Nieves, O. Chubykalo-Fesenko, P. M. Oppeneer, and U. Nowak, "Multiscale modeling of ultrafast element-specific magnetization dynamics of ferromagnetic alloys", *Phys. Rev. B* **92**, 054412 (2015).

[A.2] I. Turek, J. Kudrnovský, and K. Carva, "Magnetic anisotropy energy of disordered tetragonal Fe-Co systems from ab initio alloy theory", *Phys. Rev. B* **86**, 174430 (2012).

[A.3] I. Turek, J. Kudrnovský, and K. Carva, "Anisotropy of Magnetic Moments and Energy in Tetragonal Fe-Co Alloys from First Principles", *J. Supercond. Nov. Magn.* **26**, 1581–1584 (2013).

[A.4] F. Máca, J. Kudrnovský, V. Drchal, K. Carva, P. Baláž, and I. Turek, "Physical properties of the tetragonal CuMnAs: A first-principles study", *Phys. Rev. B* **96**, 094406 (2017).

[A.5] F. Máca, J. Kudrnovský, P. Baláž, V. Drchal, K. Carva, and I. Turek, "Tetragonal CuMnAs alloy: Role of defects", *J. Magn. Magn. Mater.* **474**, 467–471 (2019).

[A.6] K. Carva, J. Kudrnovský, F. Máca, V. Drchal, I. Turek, P. Baž, V. Tkáč, V. Holý, V. Sechovský, and J. Honolka, "Electronic and transport properties of the Mn-doped topological insulator Bi_2Te_3: A first-principles study", *Phys. Rev. B* **93**, 214409 (2016).

[A.7] K. Carva and I. Turek, "Spin-mixing conductances of thin magnetic films from first principles", *Phys. Rev. B* **76**, 104409 (2007).

[A.8] K. Carva and I. Turek, "Out-of-plane spin-transfer torques: first principles study", *J. Magn. Magn. Mater.* **322**, 1085 (2010).

[A.9] K. Carva and I. Turek, "Spin-mixing conductances: The influence of disorder", *phys. stat. sol. (a)* **205**, 1805 (2008).

[A.10] K. Carva and I. Turek, "Landauer theory of ballistic torkances in noncollinear spin valves", *Phys. Rev. B* **80**, 104432–6 (2009).

[A.11] P. Vlaic, E. Burzo, and K. Carva, "Are insulating LiF barriers relevant for spin-polarized tunnelling applications? Insights from first-principles calculations", *J. Phys. D: Appl. Phys.* **49**, 305302 (2016).

[A.12] K. Carva, P. Baláž, and I. Radu, "Chapter 2 - Laser-Induced Ultrafast Magnetic Phenomena", in *Handbook of Magnetic Materials*, Vol. 26, edited by E. Brück (Elsevier, 2017), pp. 291–463.

[A.13]   K. Carva, M. Battiato, D. Legut, and P. M. Oppeneer, "Ab initio theory of electron-phonon mediated ultrafast spin relaxation of laser-excited hot electrons in transition-metal ferromagnets", *Phys. Rev. B* **87**, 184425 (2013).

[A.14]   K. Carva, M. Battiato, and P. M. Oppeneer, "Ab Initio Investigation of the Elliott-Yafet Electron-Phonon Mechanism in Laser-Induced Ultrafast Demagnetization", *Phys. Rev. Lett.* **107**, 207201 (2011).

[A.15]   P. Maldonado, K. Carva, M. Flammer, and P. M. Oppeneer, "Theory of out-of-equilibrium ultrafast relaxation dynamics in metals", *Phys. Rev. B* **96**, 174439 (2017).

[A.16]   A. H. Reid, X. Shen, P. Maldonado, T. Chase, E. Jal, P. W. Granitzka, K. Carva, R. K. Li, J. Li, L. Wu, et al., "Beyond a phenomenological description of magnetostriction", *Nat. Commun.* **9**, 388 (2018).

[A.17]   B. Frietsch, J. Bowlan, R. Carley, M. Teichmann, S. Wienholdt, D. Hinzke, U. Nowak, K. Carva, P. M. Oppeneer, and M. Weinelt, "Disparate ultrafast dynamics of itinerant and localized magnetic moments in gadolinium metal", *Nat Commun* **6**, 8262 (2015).

[A.18]   S. Wienholdt, D. Hinzke, K. Carva, P. M. Oppeneer, and U. Nowak, "Orbital-resolved spin model for thermal magnetization switching in rare-earth-based ferrimagnets", *Phys. Rev. B* **88**, 020406 (2013).

[A.19]   M. Battiato, K. Carva, and P. M. Oppeneer, "Superdiffusive Spin Transport as a Mechanism of Ultrafast Demagnetization", *Phys. Rev. Lett.* **105**, 027203 (2010).

[A.20]   M. Battiato, K. Carva, and P. M. Oppeneer, "Theory of laser-induced ultrafast superdiffusive spin transport in layered heterostructures", *Phys. Rev. B* **86**, 024404 (2012).

[A.21]   K. Carva, "Ultrafast spintronics: Give it a whirl", *Nat. Phys. (news & views)* **10**, 552–553 (2014).

[A.22]   P. Baláž, M. Žonda, K. Carva, P. Maldonado, and P. M. Oppeneer, "Transport theory for femtosecond laser-induced spin-transfer torques", *J. Phys.: Condens. Matter* **30**, 115801 (2018).

[A.23]   M. Berritta, R. Mondal, K. Carva, and P. M. Oppeneer, "*Ab Initio* Theory of Coherent Laser-Induced Magnetization in Metals", *Phys. Rev. Lett.* **117**, 137203 (2016).

[A.24]   K. Carva, D. Legut, and P. M. Oppeneer, "Influence of laser-excited electron distributions on the X-ray magnetic circular dichroism spectra: Implications for femtosecond demagnetization in Ni", *EPL (Europhysics Letters)* **86**, 57002 (2009).

[A.25]   K. Carva, M. Battiato, and P. M. Oppeneer, "Is the controversy over femtosecond magneto-optics really solved?", *Nat Phys* **7**, 665 (2011).

[A.26]   E. Turgut, D. Zusin, D. Legut, K. Carva, R. Knut, J. M. Shaw, C. Chen, Z. Tao, H. T. Nembach, T. J. Silva, et al., "Stoner versus Heisenberg: Ultrafast exchange reduction and magnon generation during laser-induced demagnetization", *Phys. Rev. B* **94**, 220408 (2016).

Appendix A

Attached publications

(Removed from this version)